NREL
NATIONAL RENEWABLE ENERGY LABORATORY

Wind Turbine Modeling for Computational Fluid Dynamics

December 2010 — December 2012

L.A. Martinez Tossas and S. Leonardi
University of Puerto Rico
Mayaguez, Puerto Rico

NREL Technical Monitor: Pat Moriarty

NREL is a national laboratory of the U.S. Department of Energy
Office of Energy Efficiency & Renewable Energy
Operated by the Alliance for Sustainable Energy, LLC

This report is available at no cost from the National Renewable Energy Laboratory (NREL) at www.nrel.gov/publications.

NOTICE

This report was prepared as an account of work sponsored by an agency of the United States government. Neither the United States government nor any agency thereof, nor any of their employees, makes any warranty, express or implied, or assumes any legal liability or responsibility for the accuracy, completeness, or usefulness of any information, apparatus, product, or process disclosed, or represents that its use would not infringe privately owned rights. Reference herein to any specific commercial product, process, or service by trade name, trademark, manufacturer, or otherwise does not necessarily constitute or imply its endorsement, recommendation, or favoring by the United States government or any agency thereof. The views and opinions of authors expressed herein do not necessarily state or reflect those of the United States government or any agency thereof.

Abstract

With the shortage of fossil fuels and the increase of environmental awareness, wind energy is becoming more important than ever. As the market for wind energy grows, wind turbines and wind farms are becoming larger. But, there is still more to learn about this technology. For example, current utility-scale turbines extend a significant distance into the atmospheric boundary layer. Therefore, the interaction between the atmospheric boundary layer and the turbines and their wakes needs to be better understood. The turbulent wakes of upstream turbines affect the flow field of the turbines behind them, thus decreasing power production and increasing mechanical loading. With greater knowledge of this type of flow, wind farm developers could plan better-performing, less maintenance-intensive wind farms. Simulating this flow using computational fluid dynamics (CFD) is one important way to gain a better understanding of wind farm flows. In this study, we compare the performance of actuator disk and actuator line models in producing wind turbine wakes and the wake-turbine interaction between multiple turbines. We also examine parameters that affect the performance of these models, such as grid resolution, the use of a tip-loss correction, and the way in which the turbine force is projected onto the flow field. We see that as the grid is coarsened, the predicted power decreases. As the width of the Gaussian body force projection function is increased, the predicted power is increased. The actuator disk and actuator line models produce similar wake profiles and predict power within 1% of one another when subject to uniform inflow. The actuator line model is able to capture flow structures near the blades such as root and tip vortices, which the actuator disk does not capture, but in the far wake, they look similar. The actuator line model was validated using the wind tunnel experiment conducted at the Norwegian University of Science and Technology, Trondheim. Agreement between the model and the experiments was obtained, with the maximum percentage difference in power coefficients of 25% and 40% for thrust coefficient. The actuator line and actuator disk models were compared when running large-scale wind farm simulations. Normalized power was similar for both models, but dimensional power differed from 1 to 17%. The actuator disk model was able to run approximately three times faster, though. This work shows that actuator models for wind turbine aerodynamics are a viable alternative to using full blade-resolving simulations. However, care must be taken to use the proper grid resolution and force projection to the CFD grid to obtain accurate predictions of aerodynamic forces and, hence, power. More work is needed to determine the best method of body force projection onto the CFD grid.

Abbreviations and Nomenclature

ABL   Atmospheric boundary layer
ADM   Actuator disk model
ALM   Actuator line model
ASM   Actuator surface model
BEM   Blade Element Momentum
CFD   Computational fluid dynamics
DNS   Direct numerical simulation
LES   Large eddy simulation
N-S   Navier-Stokes equations
RANS   Reynolds-averaged Navier-Stokes
SGS   Subgrid-scale

C_D Drag coefficient
C_L Lift coefficient
C_P Power coefficient
C_T Thrust coefficient
p Pressure
t   Time
U Velocity
U_∞ Free stream velocity

λ Tip speed ratio
ν_{SGS} Subgrid-scale viscosity
ρ Density
σ Solidity factor
τ_{SGS} Subgrid-scale stress

iv

Table of Contents

(Unless otherwise noted, all figures/tables were created by Luis A. Martínez.)

List of Tables

List of Figures

1 Literature Review

1.1 Introduction

With the shortage of fossil fuels and the increase of environmental awareness, renewable energy is becoming more important than ever. As the market for wind energy grows, wind turbines and wind farms are growing as well. Current utility-scale wind turbines extend to a significant distance into the atmospheric boundary layer (ABL), with rotor diameters of up to 120 meters (m) and 5 megawatts (MW) installed power [1]. To design and control superior performing, less maintenance-intensive wind farms, the interaction between the ABL, the turbines, and their wakes needs to be better understood.

In the past years, wind turbine aerodynamics research has focused on acquiring high-quality experimental data and solving the incompressible Navier-Stokes equations for individual and clustered wind turbines. Often, actuator models are used to reduce grid requirements and simplify the problem. Actuator models are the subject of this thesis. The actuator disk model (ADM) represents the wind turbines as disks that impose body forces on the flow field depending on the fluid velocities. Several variations of the model exist, with some models taking only the axial direction of the imposed force into account and others taking only the axial and tangential forces into account. The actuator line model (ALM) represents the blades as a set of points along each blade axis that rotate in time. Each point defines a discrete section of the blade with its respective airfoil characteristics. The lift and drag forces on the blades are calculated based on the local velocities at each point.

1.2 Basics of Wind Turbine Aerodynamics

Wind turbines generate power by extracting kinetic energy from the wind. The following analysis is based on One-dimensional Momentum Theory. The air that passes through the turbine is contained within a stream tube. As the power is extracted the wind expands, thus increasing the cross-sectional area of the stream tube. The energy extracting device for this simple model is called an actuator disc. By definition, the mass of air passing through the stream tube is conserved. The air velocity at the disc is related to the free stream velocity by means of the induction factor

$$U_d = U_\infty(1 - a) \tag{1.1}$$

where

U_d is the velocity at the disc

U_∞ is the free stream velocity

a is the induction factor.

The momentum theory applied to a one-dimensional stream shows that power extracted from the wind is given by

$$C_p = \frac{P}{\frac{1}{2}\rho U_\infty^3 A} = 4a(1 - a)^2 \tag{1.2}$$

where

P is power

ρ is density

A is the area of the disc.

The power coefficient, C_p, is defined as the ratio of power extracted to the available power in the mean flow. Taking the derivative of C_p with respect to a allows us to find the maximum value of the function. This results in an induction factor of $a = 1/3$ and a maximum power coefficient of $C_p = 16/27 = .593$, which is known as the Betz limit [2].

1

Angular momentum theory, which takes into account the rotation of the wake, can be used to obtain the same result [3]. The thrust coefficient is another important parameter and is defined as

$$C_T = \frac{T}{\frac{1}{2}\rho U_\infty^2 A} = 4a(1-a) \tag{1.3}$$

where

T is thrust.

As the wind passes through the rotor, an aerodynamic thrust and torque are produced in the blades, which are used then to produce power. The air experiences an equal and opposite force. The increase in kinetic energy of the air due to the force exerted by the blades is compensated by a decrease in pressure. The circulation generated at the blades generates root and tip vortices. These vortices convect downstream with the local flow velocity. The vortex cylinder theory takes into account the spin of the wake, yielding a lower power coefficient. The vortex theory, even though it does not account for wake expansion, produces results that agree with the momentum theory.

Blade-element momentum (BEM) theory assumes that the forces on the blade sections may be calculated from two-dimensional (2D) airfoil data. The airfoil lift and drag coefficients are functions of the angle of attack. Wind velocity is a combination of the velocity of the wind, which accounts for axial and tangential induction, and the rotation of the rotor. BEM momentum theory states that the force exerted at each blade element is responsible for the change of momentum in the air that passes through the annulus which is swept by the element [2]. BEM theory yields results for the power coefficient as a function of tip speed ratio.

For heavily loaded turbines, the momentum theory has to be modified because of the creation of a turbulent wake. This causes a mixing process between the wake and the free stream. This mixing process re-energizes the lower energy air that has gone through the rotor.

These basic concepts are used to develop models and techniques to simulate wind turbines inside numerical codes. Simulations provide results not only for the parameters affecting the turbines such as thrust and torque, but also the properties of the wake formed behind the turbine.

1.3   Wind Turbine Computational Fluid Dynamics

In past years, wind turbine computational fluid dynamics (CFD) have been focused on solving the incompressible Navier-Stokes equations [4]. The flow in wind turbines is incompressible with velocities ranging from 5 to 25 meters (m) / seconds (s). Compressibility effects are only present at the tip because of the high velocities caused by rotation. Mach number at the tip is still fairly low ($M \leq 0.25$) so it is reasonable to assume that the flow is incompressible, even if resolving the blades. Thus the incompressible Navier-Stokes equations

$$\nabla \cdot \mathbf{u} = 0 \tag{1.4}$$

$$\frac{\partial \mathbf{u}}{\partial t} + (\mathbf{u} \cdot \nabla)\mathbf{u} = -\frac{1}{\rho}\nabla p + \nu\nabla^2\mathbf{u} \tag{1.5}$$

are suitable for wind turbine modeling.

When dealing with ABL flows, the Boussinesq approximation is typically used for buoyancy effects and an equation for temperature has to be solved. The Coriolis effect may be present when dealing with large wind turbines and wind farms. For ABL flows, the largest scales are on the order of 1 kilometer (km) while the smallest scales are on the order of 1 mm. This disparity of scales makes the option of using direct numerical simulations (DNS) not feasible because of the computational resources required. Researches have adopted Reynolds-averaged Navier-Stokes (RANS) methods to solve the mean flow. The RANS equations

$$\frac{\partial \bar{\mathbf{u}}}{\partial t} + (\bar{\mathbf{u}} \cdot \nabla)\bar{\mathbf{u}} = -\frac{1}{\rho}\nabla p + \nu\nabla^2\bar{\mathbf{u}} - \nabla \cdot (\overline{\mathbf{u}'\mathbf{u}'}) \tag{1.6}$$

2

are used where over bar denotes Reynolds decomposition $\mathbf{u} = \bar{\mathbf{u}} + \mathbf{u}'$,

and $\overline{\mathbf{u}'\mathbf{u}'}$ is the Reynolds stress tensor, which is then modeled in terms of the mean flow quantities.

Researchers in the wind energy wake community have adopted large eddy simulations (LES) in recent years. The flow over wind turbines is highly unsteady and, with the RANS equations, these unsteady features are lost due to averaging. A better approach is to use LES, in which the flow dependence in time is resolved. LES calculates the larger eddies while smaller eddies are modeled. The filtered incompressible Navier-Stokes equations used are

$$\frac{\partial \tilde{\mathbf{u}}}{\partial t} + (\tilde{\mathbf{u}} \cdot \nabla)\tilde{\mathbf{u}} = -\frac{1}{\rho}\nabla \tilde{p} + \nu \nabla^2 \tilde{\mathbf{u}} - \nabla \cdot (\widetilde{\mathbf{u}\mathbf{u}} - \tilde{\mathbf{u}}\tilde{\mathbf{u}}) \tag{1.7}$$

where

the term $(\widetilde{\mathbf{u}\mathbf{u}} - \tilde{\mathbf{u}}\tilde{\mathbf{u}})$ is often modeled by

$$\tau_{SGS} = (\widetilde{\mathbf{u}\mathbf{u}} - \tilde{\mathbf{u}}\tilde{\mathbf{u}}) = -\nu_{SGS}(\nabla \tilde{\mathbf{u}} + (\nabla \tilde{\mathbf{u}})^T) \tag{1.8}$$

and ν_{SGS} is the subgrid-scale (SGS) viscosity and is modeled using several subgrid-scale models. The filtering operation was applied at $\mathbf{u} = \tilde{\mathbf{u}} + \mathbf{u}''$.

In past years, RANS and LES have been used to simulate wind turbine flow. However, researchers are increasingly using LES because of its ability to better predict the ABL and the wake behind wind turbines.

1.4 Atmospheric Boundary Layer Simulations

The principal factors that affect the behavior of the ABL are the geostrophic wind, the surface roughness and terrain, the Coriolis effects, and thermal stratification. Thermal stratification is categorized as stable, unstable and neutral. Unstable stratification occurs when there is significant surface heating, causing the warmer air near the surface to rise. When a volume of air rises, the pressure exerted upon it decreases and it expands and cools nearly adiabatically. With respect to elevation, if the rate of cooling of the volume of air does not equal or exceed the lapse rate of the ABL (the vertical gradient of temperature), it will keep rising, resulting in enhanced vertical mixing and a thicker ABL. If the ground is cold, the vertical motion of the air will be suppressed, thus giving rise to stable stratification. Neutral stability occurs as the wind reaches thermal equilibrium with its surroundings as it rises.

To mimic the ABL for wind turbine wake simulations, the boundary conditions of the flow need to be prescribed. Different boundary conditions are used to simulate ABL scenarios such as the sheared velocity profile, the anisotropy of the turbulence, and the instationary nature of the flow. The bottom surface is usually described as a no-slip boundary condition or a wall function to account for roughness. At the upper boundary, stress and flux-free conditions are usually employed. In the streamwise direction periodicity is usually employed to simulate infinite wind farms or as a precursor to generate the ABL turbulence. Periodicity conditions are convenient from a numerical point of view due to the application of fast solvers.

Porté-Agel et al. [5] performed an LES of the ABL with wind turbines. The SGS stresses and heat flux were modeled using tuning-free, scale-dependent Lagrangian dynamic models. They compared the results with experimental data from a wind tunnel at the St. Anthony Falls Laboratory using miniature wind turbines. The LES code solved the filtered continuity equation, the filtered momentum equations (in rotational form), and the filtered temperature transport equation. Buoyancy effects were taken into account by means of the Boussinesq approximation. The deviatoric part of the SGS model was calculated using an eddy viscosity model while the SGS heat flux model used an eddy-diffusivity model. The scale-dependent Lagrangian dynamic SGS models implemented take into account the anisotropy of the flow by dynamically adjusting the Smagorinsky coefficient. The surface shear and heat flux at the bottom were calculated by means of the Monin-Obukhov theory using instantaneous (filtered) fields. The upper boundary condition was a stress- and flux-free condition.

Calaf et al. [6] used a pseudo-spectral code to model the ABL. This study focused on investigating a fully developed wind-turbine-array boundary layer. Two different LES codes were used. One method used the skew-symmetric

form of the Navier-Stokes equations, with a pseudo-spectral discretization with periodic boundary conditions in the horizontal direction and centered second-order finite differencing in the vertical direction. The second code used a pseudo-spectral discretization in the horizontal direction but fourth order energy-conservative finite difference discretization in the vertical direction. Time integration was done using the fourth order Runge-Kutta scheme. The standard Smagorinsky sub-grid model was used in both cases. The roughness height was approximated using Lettau's formula. The flow used was fully developed and driven by means of an imposed pressure gradient. The turbulent kinetic energy vertical fluxes were of the same order of magnitude as the power extracted by the wind turbines. The study focused on equivalent roughness models of wind farms and proposed that the modified Frandsen formula to calculate the roughness height of the wind farm.

In their study, Troldborg et al. [7] used the three-dimensional (3-D) flow solver, EllipSys3D, developed by Mikkelsen and Sørensen. The code solved the incompressible Navier-Stokes equations in general curvilinear coordinates using a block structured finite-volume approach. The SGS viscosity was modeled by means of the vorticity-based mixed-scale model by Ta Phuoc et al. [8]. The pressure was solved by means of the Pressure Implicit with Splitting of Operators algorithm.

When doing large eddy simulation (LES) of the ABL, the spatial resolution is such that it does not fully resolve the blade geometry of a wind turbine. It is impossible to fully resolve the flow in the ABL and around a wind turbine at the same time, especially considering the computational resources that are currently available. This is the main reason to develop wind turbine actuator models that can simulate wind turbines without having to resolve the full geometry.

1.5   Actuator Disc Model (ADM)

The ADM simulates the turbine as a disc within the flow that imposes forces on the fluid. Many versions of the ADM exist. Some apply thrust and tangential forces while others only apply thrust. Many researchers have adopted the ADM for simulating wind turbines. Even though the ADM may simulate the turbines and their wakes, it does not create the tip vortices that are carried onto the wake [9].

Porté-Agel et al. [5] compared two different versions of the ADM: the ADM that applies both thrust and tangential force and the one that applies only thrust. The actuator disk model, with no tangential force, is based on the momentum theory of propellers. The actuator disk force is distributed uniformly over the circular disc. The force exerted on the disc is given by:

$$T = \frac{1}{2}\rho \tilde{u}_0^2 A C_T \tag{1.9}$$

where

T is the thrust force

ρ is the density

$\tilde{u}_0^2$ is the unperturbed resolved velocity of the axial incident flow in the center of the rotor disk

A is the rotor swept area

C_T is the thrust coefficient.

This model presents a one-dimensional approximation of the thrust force and does not take into account the rotation in the flow produced by the blades. It also does not seem to take into account radial variation of T.

The ADM, with tangential force, is implemented by integrating the lift and drag by the blades over the spatial and temporal resolution used in the LES. The force implemented by the actuator disc model (vectors are in bold) is given by:

$$\mathbf{f}_{2D} = \frac{d\mathbf{F}}{dA} = \frac{1}{2}\rho V_{rel}^2 \frac{Bc}{2\pi r}(C_L \mathbf{e}_L + C_D \mathbf{e}_D) \tag{1.10}$$

4

where

B is the number of blades

V_{rel} is the local velocity

C_L is the lift coefficient

C_D is the drag coefficient

c is the chord length

and $\mathbf{e}_L$ and $\mathbf{e}_D$ are the unit vectors in the direction of lift and drag, respectively.

Calaf et al. [6] used the ADM in their study. The wind turbines were modeled by means of the âĂIJdrag diskâĂİ concept. The momentum equation had an extra term for the thrust force of the turbines. The velocity used for the model was averaged over the disk region. The total force was distributed among all the grid points that fell into the wind turbine disk region. The grid spacing was uniform in all directions.

The wind turbine model used the classic model for one directional force:

$$T = -\frac{1}{2}\rho C_T U_\infty^2 \frac{\pi}{4} D^2,$$ (1.11)

where

C_T is the thrust coefficient

and U_∞ is the upstream undisturbed reference velocity.

The values for the thrust coefficients used are $C_T = .75$ and the induction factor $a = 1/4$, which can be found in existing wind turbines. The force is calculated by averaging the velocity throughout the area swept by the actuator disk. The force is distributed on each cell and depends on the frontal area of the cell, which coincides with the area of the disc. The forces at each cell are distributed among surrounding cells by means of a Gaussian convolution filter.

In their work, Ammara et al. [10] used the ADM and solved the Navier-Stokes equation with a control-volume finite element method. Axial and tangential forces were taken into account in the model as well as a tip correction factor, to account for blade tip effects. The calculations were compared to experimental data from the US Department of Energy MOD-0A rotor and MOD-2 cluster, where an acceptable level of accuracy was obtained in terms of wake velocity predictions and wind farm performance.

Jimenez et al. [11] implemented the ADM into a CFD code based on a LES approach. The ADM model used accounted only for thrust forces, thus neglecting rotational effects. The force imposed on the flow was:

$$T = -C_T \frac{1}{2} A u_0^2$$ (1.12)

where

C_T is the thrust coefficient of the turbine

A is the frontal area of the cell

and u_0 is the unperturbed velocity of the incident flow at the center of the disk.

The velocity profile incident over the turbine agreed with the logarithmic law, while the velocity value in the upper part of the domain was larger than what the law of the wall provided. Discrepancies between computations and measurements in the turbulence intensity of the wakes were found in the flow direction.

Masson et al. [12] performed simulations using the actuator disc concept. The tower was modeled in a similar manner as a permeable wall. The model was tested using a 3D Cartesian and an axisymmetric polar solver and was

compared to the Tjaereborg turbine. In addition, the National Renewable Energy Laboratory (NREL) combined experimental rotors obtaining good results. Discrepancies were attributed mostly to the turbulence and dynamic stall modeling.

Mikkelsen et al. [13] used an actuator disk model to investigate the effects of rotor coning. In the model, blade element momentum was used to calculate the forces of the blades imposed on the fluid. For the coned rotor, the interference factors were found to change considerably with the radius of the disc. It was shown that BEM theory under-predicts the blade-root shear and power coefficients by up to 7%.

The ADM provided reasonable overall results, however there are still many things to improve. For example, the forces imposed on the fluid were averaged through the rotor whereas the actual forces acted only in the instantaneous location of the blades. The ADM was not able to capture tip vortices, which are important when studying the near wake of a wind turbine. With these limitations, researchers have devised other models which improve the results provided by the ADM.

1.6 Actuator Line Model (ALM)

The ALM models the wind turbine blades as a set of blade elements along each blade axis. The model uses airfoil data to calculate lift and drag at each element and applies to the flow field as body forces. The ALM does not resolve the full geometry of the blades.

Sørensen et al. [14] implemented the ALM to study the dynamics of the wake and the tip vortices. The body forces were calculated based on tabulated airfoil data. The total force on a blade element is:

$$\mathbf{f}_{2D} = \frac{\mathbf{dF}}{dA} = \frac{1}{2}\rho U_{rel}^2 c(C_L\mathbf{e}_L + C_D\mathbf{e}_D) \tag{1.13}$$

where

C_L and C_D are the lift and drag coefficients

U_{rel} is the local wind velocity

and $\mathbf{e}_L$ and $\mathbf{e}_D$ are the unit vectors in the direction of lift and drag, respectively.

The blade element forces are projected using a convolution:

$$\mathbf{f}_\varepsilon = f \otimes \eta_\varepsilon \tag{1.14}$$

where

η_ε is a regularization function.

They use a Gaussian given by:

$$\eta_\varepsilon = \frac{1}{\varepsilon^3 \pi^{3/2}} \exp[-(r/\varepsilon)^2] \tag{1.15}$$

where

ε establishes the width of the function. The model was validated by comparing power output data from the Nordtank turbine.

Ivanell et al. [15] used direct numerical simulations to study the wakes behind a wind turbine. The turbine was represented by using the actuator line model. Tabulated airfoil data, was then used to calculate the body forces imposed on the fluid. This study paid special attention to the tip vortices. The solver used a finite-volume discretization of the Navier-Stokes equations in general curvilinear coordinates. The Reynolds number, based on inflow velocity and rotor radius, was 50,000, with a mesh of about 5 million grid cells. The body forces imposed on the fluid by the turbine

model were projected by means of a Gaussian convolution. This study also used a 2D convolution on the plane orthogonal to the actuator line. The results were compared to the Tjaereborg turbine, with a 10 m/s wind speed and a tip speed ratio of 7. It was found that the circulation along the blades was nearly constant.

Troldborg et al. [7] performed large eddy simulations using the ALM with the vorticity-based mixed-scale model by Ta Phuoc. The model was compared to field measurements of the Tjaereborg turbine and obtained agreement. It was observed that the far wake followed an axial velocity distribution resembling a Gaussian shape. The regularization parameter ε was studied by finding an optimum value where the forces were projected in such a way that the model was able to capture root and tip vortices. The discrepancies in the model were attributed to the inaccuracy of the 2-D airfoil data and to the non-inclusion of the nacelle in the model.

Mikkelsen et al. [16] performed studies on multiple turbines using the ALM. The model was tested on a row of turbines with pitched blades. The wakes interacted in a fully unsteady nonlinear manner. In his Ph.D. thesis, Mikkelsen investigated the ALM in detail in a finite volume solver using pressure-velocity formulation in curvilinear coordinates [17].

In his Ph.D. thesis, Troldborg performed a detailed study of the ALM [9]. The ALM model was tested for different tip speed ratios showing different wake developments. Power coefficient comparisons with measured data showed good agreement. Discrepancies were attributed to inaccurate airfoil data. When subjected to shear-flow, the non-symmetric rotor loading caused a skewed wake development. When subjected to non-sheared turbulent inflow, the wake broke up quickly, thereby increasing turbulence levels in the wake. As the wake progressed in sheared and turbulent flow, the asymmetry gradually diminished. When studying three turbines in a row, the turbulent case caused higher inflow velocities on the downstream turbines due to the faster wake recovery. When studying two turbines in a row under the ABL that was characterized by strong shear and low-ambient turbulence, the second turbine experienced tilt moment caused by the wind shear and severe yaw moments. The wake of the first turbine did not break up before reaching the second one, resulting in a complex inflow for the second turbine.

The ALM yielded accurate results but it still had limitations. Each blade-element force was the total force over that element, whereas the real forces were distributed smoothly over the chord of the blade-element. To distribute the blade element point force, a Gaussian projection was used, which eliminated numerical instabilities but did not reproduce the actual force distribution on the blades. Other projections are possible, though.

1.7   Actuator Surface Model (ASM)

Another model that has been explored recently is the ASM. This model calculates the forces on a 2-D airfoil as a function of the chord, thus avoiding one of the major simplifications of the ALM. This is done by using empirical formulas with forces as a function of the chord position. Shen et al. [18] investigated the ASM on a NACA0015 airfoil. The model predicts accurate results using a 2 dimensional Navier-Stokes incompressible solver. In a vertical axis wind turbine, the model failed to accurately predict the normal and tangential forces. This was improved by using the Leishman-Beddoes dynamic stall model.

Dobrev et al. [19] discussed the application of an actuator surface hybrid model. The model uses blade-element momentum theory (BEM) in a computational fluid dynamics (CFD) solver. The model was implemented using Fluent CFD package. The results were compared with the NREL Phase VI experiment data and showed satisfying agreement. It was noted that it is important to employ a correction for the circulation distribution near the tip region as well as the induced velocity angles.

In their study Watters et al. [20] conducted a more thorough investigation of the ASM. Two- and three-dimensional versions of a control-volume finite element method model were used to compute inviscid flow. The ASM produced accurate results when compared to the Prandtl lifting model. The model was validated using the wind turbine rotor of the Technical University of Delft and obtained encouraging results. The flow structures inherent to a vortical wake were well reproduced. The model can be used to simulate propellers, helicopters and wind turbines. Furthermore, integration of viscous drag in the model is a subject of interest that could be explored to help improve the model.

The ASM is a promising approach for modeling wind turbines in CFD solvers. The model's main advantage is its ability to provide a more realistic force distribution. The limitation of the ASM is its dependency on an external calculation for the force distribution as a function of position within the chord of an airfoil.

1.8 Comparison Between ADM and ALM

Porté-Agel et al. [5] compared the ADM that calculates thrust and tangential forces (ADM-R), the ADM that imposes only thrust force (ADM-NR), and the ALM. The ALM calculates lift and drag for discrete sections of the blade and distributes them along the blades. The ALM, as opposed to the ADM, captures tip vortices and coherent periodic helicoidal structures in the near-wake region. The turbine induced force is

$$\mathbf{f}_{2D} = \frac{\mathbf{dF}}{dA} = \frac{1}{2}\rho V_{rel}^2 c(C_L\mathbf{e}_L + C_D\mathbf{e}_D) \tag{1.16}$$

The forces in these models are projected smoothly onto the flow field to avoid singular behavior and numerical instability. The forces are projected by means of a Gaussian distribution. The nacelle and tower are modeled as drag forces and include their respective drag coefficients.

The numerical models were compared to experimental results from wind tunnel measures at the Saint Anthony Falls Laboratory. The turbine wakes were characterized using the streamwise velocity and the streamwise turbulence intensity. The ALM and the ADM-R were in agreement with the experimental data. The ADM-NR yielded a poor prediction of the mean velocity distribution.

The maximum turbulence intensity in the experiments was found near the top tip at a normalized distance of 3 to 5 diameters downstream. The numerical models captured different turbulent intensities, but the ADM-R and the ALM were in agreement with the experimental data.

The ALM was implemented into an LES code for a stable boundary layer. The model was able to capture blade-induced 3-D helicoidal tip vortices. As stated by previous studies, the results showed that wind farms create an impact on local meteorology.

1.9 Conclusions

In the past years, wind turbine aerodynamic research was focused on solving the incompressible Navier-Stokes equations. Not until recently have people done real ABL simulations with turbines. It is much more common for people to use a general (not ABL-specific) solver by applying stochastic turbulence at the inlet to try to simulate ABL flow. Often, the turbines are modeled using several actuator models, thereby eliminating the need to resolve the full geometry of the blades. The ADM simulates the turbines as a permeable disc in the flow field and can yield good results if tangential forces are taken into account. The ALM represents the turbine blades as lines that impose body forces on the fluid, thereby yielding accurate results. The ASM represents the blades as 2-D actuating surfaces that impose body forces on the flow field.

Future research efforts will be aimed at simulating wind farms and aeroelastic coupling between the flow field and the turbines [1]. The behavior of the wake, and the interaction between wakes in the ABL flow, are not fully understood yet. These challenges will be a motivation for researchers to achieve better modeling of wind turbine aerodynamics.

2 Actuator Turbine Model Implementation

The actuator disk model (ADM) and actuator line model (ALM) predict blade forces depending on the local fluid velocity at each actuator element. These forces are then projected onto the flow field as body forces and imposed into the Navier-Stokes equations. The forces calculated in the models are point forces for individual blade sections. To distribute point forces onto the surrounding volume, the forces are projected by means of a Gaussian function

$$\vec{\mathbf{f}}_{turb} = \frac{\vec{F}}{\varepsilon^3 \pi^{3/2}} exp[-(r/\varepsilon)^2] \tag{2.1}$$

where

$\vec{\mathbf{f}}_{turb}$ is the projected body force per unit volume

$\vec{F}$ is the force at the actuator element

ε establishes the projection width

and r is the distance from the location of the actuator element center to the point where the force is applied.

The function decays to 1% of its maximum value when $r = 2.15\varepsilon$.

The models calculate blade quantities such as angle of attack, lift, and drag by using the local velocity at each actuator point. The local angle of attack is taken to be the angle between the chord and the local flow. This assumption is made knowing that the actuator point lies within the center of the bound vortex where the effects of up- and down-wash are small. Tabulated airfoil data are used to obtain the lift and drag coefficients. Power output is calculated by integrating the torque created with respect to the center of the rotor, and multiplying it by the rotational speed of the rotor.

2.1 Actuator Line Model

The geometry of the wind turbine is defined in a Cartesian coordinate system. The geometry of the turbine is created based on three key point locations: nacelle, hub and ground. The nacelle point is connected to the ground point by a vertical line. The hub point is connected to the nacelle point with a line defined by the turbine's yaw angle into the wind, and the tilt angle between the horizontal plane and the nacelle axis. This is the line about which the blades rotate. The blades are defined as a series of points along each blade's axis and each point is the center of an actuator element. The first blade is defined as a line parallel to the ground (x-y) plane. The other blades are created by using a rotation matrix as follows:

$$\begin{bmatrix} u_x^2 + (1-u_x^2)c & u_x u_y(1-c) - u_z s & u_x u_z(1-c) + u_y s \\ u_x u_y(1-c) + u_z s & u_y^2 + (1-u_y^2)c & u_y u_z(1-c) - u_x s \\ u_x u_z(1-c) - u_y s & u_y u_z(1-c) + u_x s & u_z^2 + (1-u_z^2)c \end{bmatrix} \begin{bmatrix} x_0 \\ y_0 \\ z_0 \end{bmatrix} = \begin{bmatrix} x_1 & y_1 & z_1 \end{bmatrix} \tag{2.2}$$

where

$c = cos(\theta)$ and $s = sin(\theta)$

$\vec{u} = u_x\vec{e}_x + u_y\vec{e}_y + u_z\vec{e}_z$ is the unit vector normal to the plane of rotation

θ is the angle of rotation, x_0, y_0, and z_0 are the coordinates of the point to be rotated

and x_1, y_1, and z_1 are the coordinates of the rotated point.

The blades are rotated at each time step by using the angular speed of the rotor. The locations of all the points along each blade are rotated using the rotation matrix in Equation 2.2. Figure 1 shows a schematic of the ALM, and the left side of Figure 2 is an example of the wake and vortex system it creates. The figure shows a horizontal contour plane through the hub of streamwise velocity.

The actuator line points define the location of different sections of the blades that have a specific lift and drag depending on their airfoil type, twist angle, chord length, and incoming flow conditions. A lift and drag resultant body force vector can be assigned to each actuator line point. The body force equal and opposite to the lift and drag is imposed in the momentum equation. The lift and drag are calculated based on the local wind speed and angle of attack:

$$L = \frac{1}{2}C_L(\alpha)\rho V^2 cw \tag{2.3}$$

$$D = \frac{1}{2}C_D(\alpha)\rho V^2 cw \tag{2.4}$$

where

α is the local angle of attack with respect to the chord

$C_L(\alpha)$ is the lift coefficient

$C_D(\alpha)$ is the drag coefficient

ρ is the densiy

V is the local wind speed

c is the chord

and w is the width of the section.

These forces are then projected onto the flow field by means of the Gaussian function shown in Equation 2.1.

The plane where the body force vector lies is perpendicular to the actuator lines, as shown in Figure 3. The planes are created by defining two new vectors: x' and y'. The cross product of the directional vector of the actuator line, z', and the vector around which the blades rotate gives the resultant directional vector pointing in the tangential direction of rotation of the blades y'. The cross product of the new vector y' and the z' vector gives the vector x', which is also used to define the plane where the forces lie. The new set of vectors is updated every time step, for each blade, according to the rotation of the blades. The velocity vector is projected onto the new plane by means of the dot product.
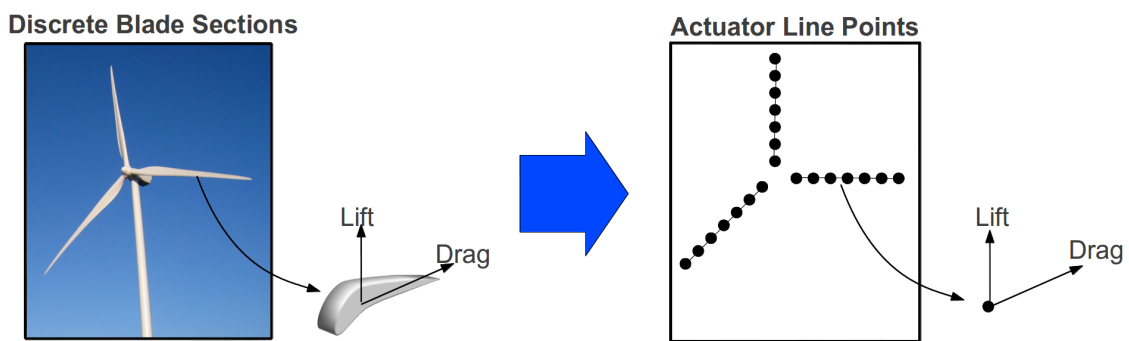
Figure 1. A schematic of an actuator line turbine model

2.2   Actuator Disk Model

The ADM simulates the turbine blades as a disk inside the flow field that occupies the swept area of the blades. This is done by dividing the rotor swept area into many elements. The geometry of the ADM is similar to the ALM. The

10
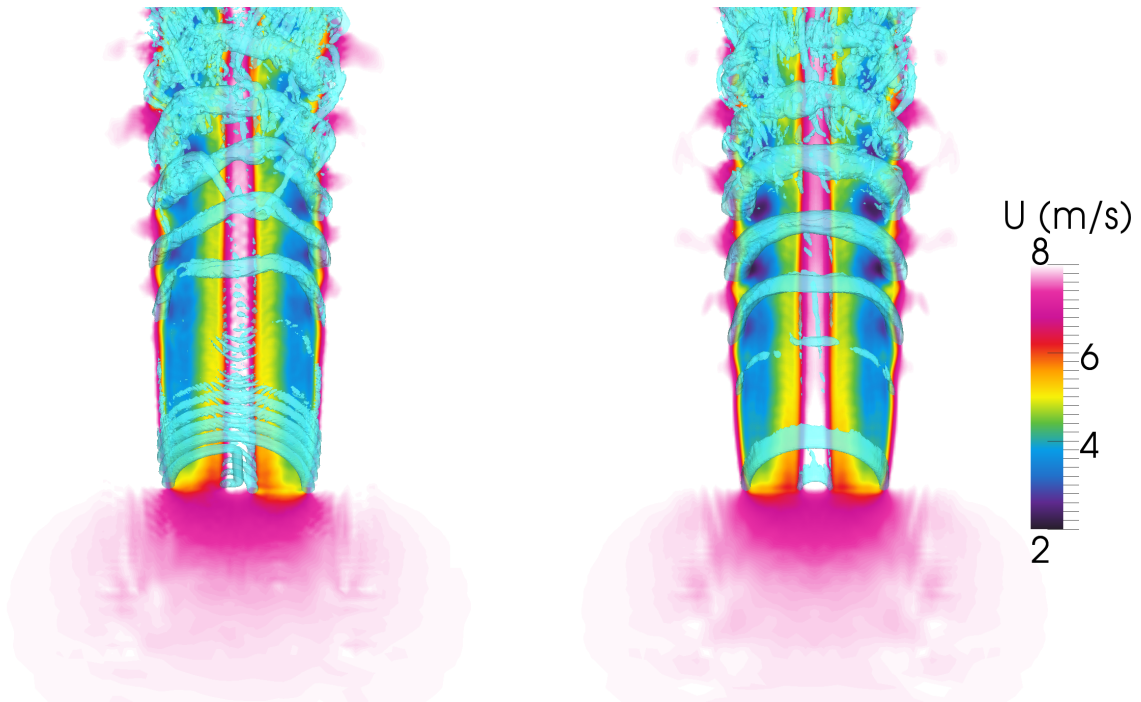
Figure 2. Actuator line model (left) and actuator disk model (right) simulations where the blue isosurface is of the second invariant of the velocity-gradient tensor. The contours are of streamwise velocity.
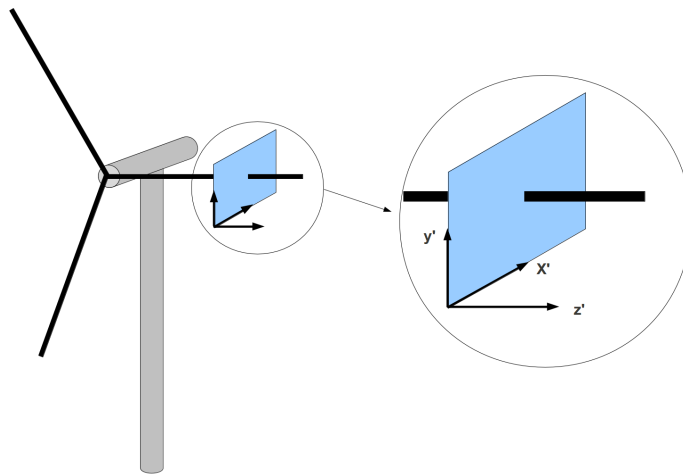
Figure 3. Plane onto which the velocity vector is projected

difference is that there are as many actuator lines as there are circumferential sections. Each point now represents a section of the disk. Figure 4 shows the schematic of an ADM where each actuator point represents an element in the disk. In addition, the right side of Figure 2 shows an example of the wake and vortex system created by the ADM. The force at each element is scaled by a solidity factor:

$$\sigma = \frac{NA_B}{A_r} \tag{2.5}$$

11

where

N is the number of blades

A_B is the area of an individual section

and A_r is the swept area of the blades.

The lift and drag forces on each actuator disk element are given by

$$L = \sigma \frac{1}{2} C_L(\alpha) \rho V^2 cw \tag{2.6}$$

$$D = \sigma \frac{1}{2} C_D(\alpha) \rho V^2 cw \tag{2.7}$$
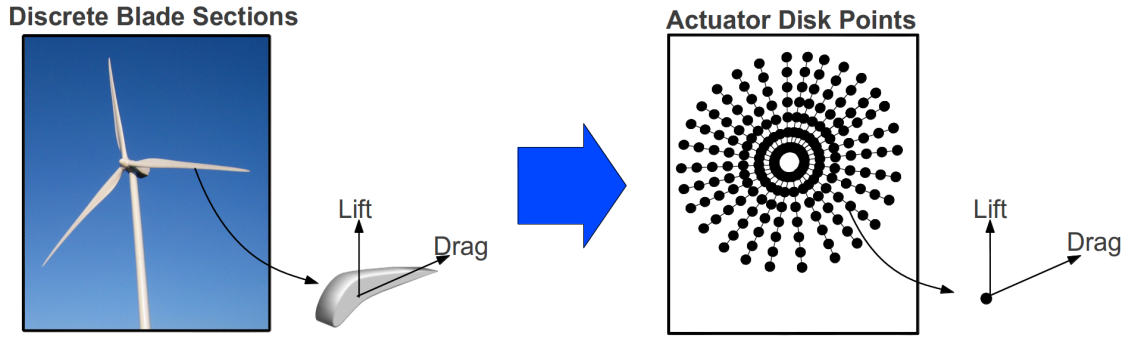
Figure 4. A schematic of an actuator disk turbine model

2.3 Numerical Method

To use the ADM and ALM, a CFD solver is used. We implemented the solver using the OpenFOAM (Open Field Operation and Manipulation) toolbox [21]. The OpenFOAM package is a set of C++ libraries meant for solving partial differential equations. The turbine models were implemented as C++ classes called by the solver. A finite-volume approach is used to discretize the governing equations. The filtered Navier-Stokes equations are solved along with the standard Smagorinsky [22] model.

The large eddy simulation (LES) code solves the incompressible Navier-Stokes equations. The flow around wind turbines is incompressible, with velocities ranging from 5-25 meters per second (m/s). The incompressible filtered Navier-Stokes equations

$$\nabla \cdot \tilde{\mathbf{u}} = 0 \tag{2.8}$$

$$\frac{\partial \tilde{\mathbf{u}}}{\partial t} + (\tilde{\mathbf{u}} \cdot \nabla)\tilde{\mathbf{u}} = -\frac{1}{\rho}\nabla \tilde{p} + \nu \nabla^2 \tilde{\mathbf{u}} - \nabla \cdot \tau_{SGS} + \overrightarrow{\mathbf{f}}_{\mathbf{turb}} \tag{2.9}$$

are suitable for wind turbine modeling,

where

$\tilde{\mathbf{u}}$ is the filtered velocity vector

$\tilde{p}$ is the filtered pressure

12

ν is the kinematic viscosity

$\vec{\mathbf{f}}_{turb}$ is the turbine force

$$\nabla \cdot \tau_{SGS} = -\nu_{SGS}(\nabla\tilde{\mathbf{u}} + (\nabla\tilde{\mathbf{u}})^T)$$

and ν_{SGS} is the subgrid-scale viscosity and is modeled using the Smagorinsky subgrid-scale model.

3   Actuator Disk and Actuator Line Models in Uniform Nonturbulent Inflow

The accuracy of the actuator disk model (ADM) and actuator line model (ALM) in predicting aerodynamic forces, torque, and power production depends largely on grid resolution and the projecting function. To study these parameters, we performed a grid resolution study. The solution was compared to the results that were from the NREL-developed WT_Perf [23] code, which uses blade-element momentum (BEM) theory. Cases were studied with different values of the parameter ε, which establishes the width of the Gaussian projecting function

$$\vec{f}_{turb} = \frac{\vec{F}}{\varepsilon^3 \pi^{3/2}} \exp[-(r/\varepsilon)^2]. \tag{3.1}$$

All the meshes were created by starting with a background grid of 16.8-meter (m) resolution. Regions of successive refinement were introduced into the background grid to provide higher resolution around the turbine and wake. Each refinement region was created by splitting cells in half in each direction within that region. Three different grids were made, each with a different resolution that was local to the turbine and wake. Those turbine/wake-local resolutions were $\Delta x = \Delta y = \Delta z =$ 4.2 m, 2.1 m, and 1.05 m. The domain was 10 rotor diameters (D) wide in all directions with the turbine rotor placed in the geometric center of the domain. The finest region extended 1 diameter upstream of the turbine and 5 diameters downstream. It extended 1 diameter beyond the edge of the rotor in the other two directions. Figure 5 shows the mesh for a case that has three successive local refinements for a resolution of 4.2 m. Cases were run for four different values of the ε parameter, ranging from 4.2 m to 10.5 m. The ALM case, with $\varepsilon = 8.4$ m, was tried with and without the Glauert tip loss correction [24]. Cases for the ALM that had different number of actuator elements per blade span and cases with different time-step were run with a grid resolution of 2.1 m and $\varepsilon = 8.4$ m.
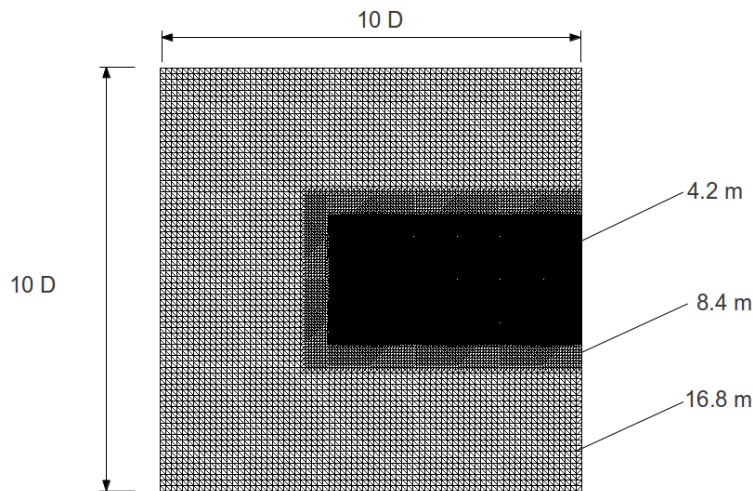
Figure 5. Domain and mesh that has a turbine/wake-local resolution of 4.2 m. The turbine is placed in the center of the domain.

3.1   Five Megawatt Reference Turbine

The turbine modeled was the 5-megawatt (MW) reference turbine designed by Jonkman et al. [25]. This horizontal-axis, upwind turbine has three blades with a rotor diameter of 126 m, a hub height of 90 m, a rated wind speed of 11.4 meters per second (m/s), and 5-MW-rated power production. Simulations were performed with an inflow

14

condition of 8 m/s. The rotational speed of the rotor was fixed at 9.1552 revolutions per minute giving a tip speed ratio of 7.55, which happens to be this turbine's normal Region 2 tip speed ratio. We chose these conditions because they provide the optimum power coefficient of the turbine, and thereby extract maximum energy from the flow. This is when the wakes are strongest and the wake effects are the most important.

3.2 Actuator Line Model

Power output predicted by the ALM is shown in Figure 6 as a function of grid resolution. The power output increases as the grid is refined. As ε becomes larger, the predicted power increases. The larger the ε value, the smaller the rate of change of predicted power as a function of grid resolution. When $\varepsilon = 4.2$ m, the difference in power predicted on the finest grid and the coarsest grid is 300 kilowatts (kW). When $\varepsilon = 10.5$ m, the difference is 40 kW, which is much smaller. Power production is clearly more grid-dependent for smaller values of ε. Simulations for $\varepsilon = 2.1$ m were run with grid resolution of $\Delta x = 1.05$ m and 0.525 m. This value of ε is limited to a minimum grid resolution of 1.05 m because numerical instabilities appear when $\varepsilon < 2\Delta x$. The trend is followed by showing that a smaller ε will produce less power. The BEM solution for power output is 1.926 MW. This value falls between the finest cases with $\varepsilon = 4.2$ and 2.1 m.

Figure 7 shows time-averaged angle of attack as a function of blade length. The difference in angle of attack provides different lift and drag coefficients, thus predicting a different force on the blades and causing different power outputs. The axial velocity at the actuator element center points is shown as a function of blade length in Figure 8. It appears that a larger ε causes less axial induction at the actuator element center points (where velocity is sampled and angle of attack is computed) and also causes more power production because the force is too smoothed out.

Velocity profiles through the wake along a horizontal line 1 diameter downstream at the hub height are shown in Figure 9. For the cases of $\varepsilon \leq 6.3$ m and $\Delta x = 4.2$ m, the profiles have a different shape compared to all other cases. When $\varepsilon / \Delta x \geq 3/2$, the resolution Δx becomes important, and we can observe instabilities in the results. The instabilities are greater near the outmost portion of the blades where the forces are greater. We observe small differences for each resolution and as the ε parameter becomes larger, these differences become even smaller. A grid resolution of $\Delta x = 2.1$ m appearss to provide converged wake profiles for each value of ε. Figure 10 shows wake profiles 4 diameters downstream. The profiles for the case of $\varepsilon = 4.2$ m and $\Delta x = 4.2$ m are affected by the numerical instabilities near the rotor, which are smoothed further downstream.

Mean wind speed and vorticity magnitude contours are shown in Figure 11 through Figure 16. The simulations in Figure 11 and 12, when $\varepsilon = 4.2$ m, are subject to numerical instabilities. These instabilities are due to the fact that $\varepsilon / \Delta x = 1$, where there is the limitation that $\varepsilon \geq 2\Delta x$ for an oscillation-free solution. The velocity in the center of the wake is greater than at larger radii. This is expected; because the hub and nacelle are not included in the model, the difference in velocity is the effect of the blades only. The blades are also not as loaded at the root as they are farther outboard, so they do not decelerate the flow there as much. Mean speed profiles are similar for different values of ε. The main difference observed is in the middle of the wake, where there is a jet. A larger value of ε projects the forces further beyond the root, leaving a small gap between the blades for the jet to form. This leaves less space for the jet as the ε value is increased. As the ε value is decreased the shear layer becomes thinner and more unstable at the rotor tip and root, causing a faster transition to turbulence. This effect is illustrated in Figure 14, which shows that a smaller value of ε produces more vorticity. The structure of the instantaneous ALM wake is not symmetric with respect to the center of the wake because the vortical structures produced by individual blades are helical and asymmetric across the wake. This asymmetry causes asymmetric roll-up of Kelvin-Helmholtz-like instabilities in the outer shear layer of the wake. As the grid is refined, vorticity contours show more structures that are filtered in coarser grids.

3.3 Actuator Disk Model

Power output predicted by the ADM is shown as a function of grid resolution in Figure 6. Power output increases as the grid is refined for all cases, similar to the ALM. Wind speed profiles through a horizontal line that are 1 diameter

This report is available at no cost from the National Renewable Energy Laboratory at www.nrel.gov/publications.

downstream at hub height are shown in Figure 9. For the case with $\Delta x = 4.2$ m and $\varepsilon = 4.2$ m, the solution has numerical oscillations, similar to the ALM. The case with $\Delta x = 4.2$ m and $\varepsilon = 6.3$ m has a different shape near the edge of the wake compared to the more refined cases. As in the ALM, this is caused by the numerical instabilities near the tip of the blade. Wake profiles shown in Figure 10 appear to converge for all resolutions, except when $\Delta x = 4.2$ m and $\varepsilon = 4.2$ m. This is due to the numerical instabilities near the rotor, as in the ALM cases.

Mean wind speed and vorticity contours for cases with $\Delta x = 2.1$ m are shown in Figures 13 and 14. Mean wind speed contours are similar to the ones for the ALM. Vorticity contours show the turbulent structures near the edge of the wake that are caused by the shear layer. As the value of ε becomes smaller, the shear layer is stronger, thus increasing the turbulence in the wake (similar to what happens in the ALM). There is no formation of tip- and root-vortices when using the ADM. These structures are formed because the bound circulation of each blade is shed at the tips in the form of vortices. A continuous disk covering the swept area of the blades does not have discrete tips on which vortices are shed. The wake is symmetric with respect to the center of the wake. This is due to the fact that the rotor is modeled as a continuous disk, rather than as individual blades. There are no asymmetric helical tip-vortices to cause asymmetric Kelvin-Helmholtz-like transition to turbulence.
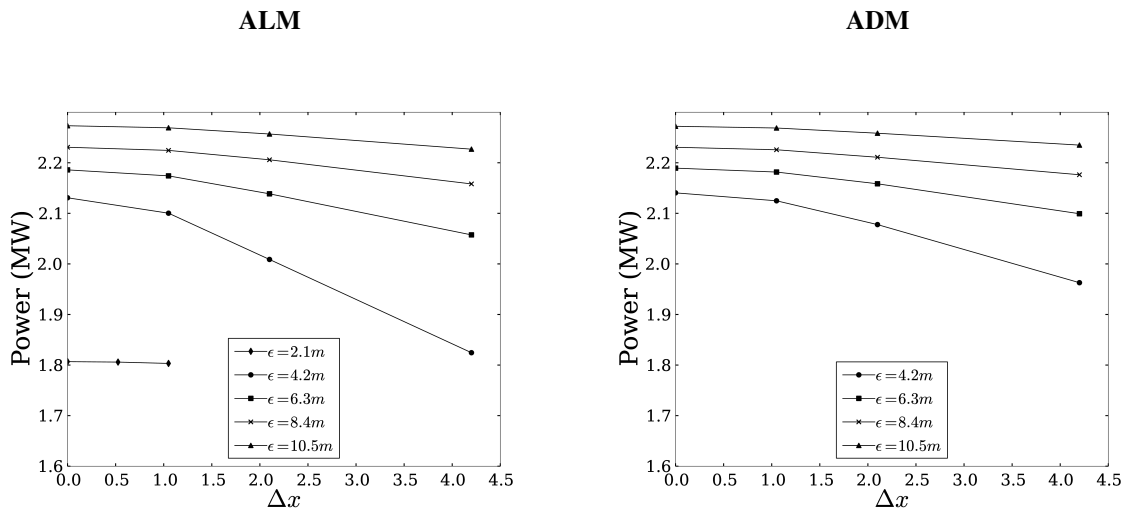
ALM   ADM

Figure 6. Power output as a function of grid resolution for different ε values

3.4   Actuator Points

Power output is shown as a function of blade segment resolution with, $\varepsilon = 8.4$ m in Figure 17. The actuator points are distributed uniformly along the blade. The resolution of the blade is presented in terms of the grid resolution $(\Delta b / \Delta x)$, where Δb is the width of the discrete blade section and Δx is the grid resolution. The number of blade sections should be high enough to predict a smooth body force field along the blades. This criterion should be the basis for establishing the blade resolution. A value of $\Delta b / \Delta x = 3$ did not predict a smooth transition through the blade, thus, the solution is not reliable. Values below $\Delta b / \Delta x = 1$ predict smoothed forces along the blade. The power output appears to converge after reaching a value of $\Delta b / \Delta x = 0.5$.

3.5   Tip Loss Correction

Figure 18 shows power output as a function of grid resolution for $\varepsilon = 8.4$ m, with and without a Glauert tip- and root-loss correction [24]. The use of a tip- and root-loss correction makes the lift go to zero more gradually at the
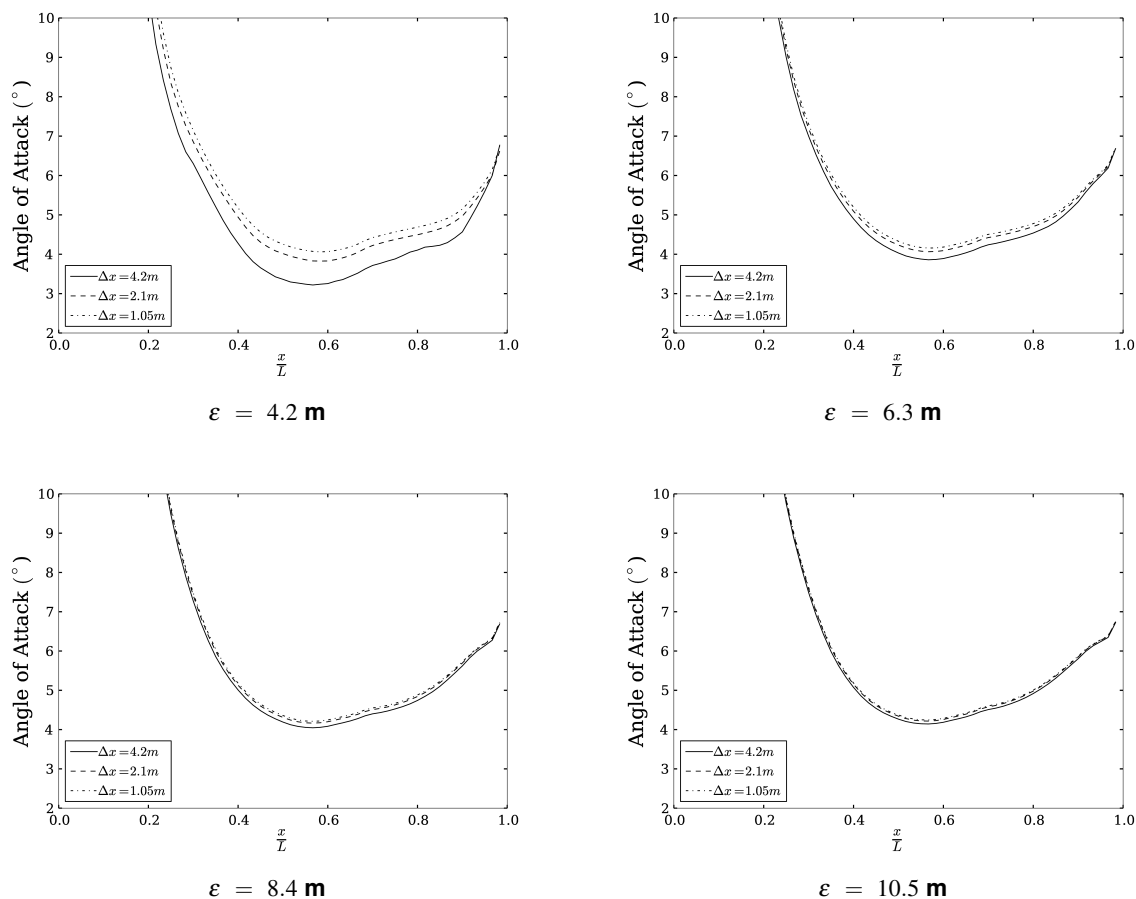
16

Figure 7. Angle of attack as a function of blade length for the ALM

tip and root of the blade. This correction decreases the total force on the blade, creating less torque, which results in lower power production. Figure 18 illustrates this effect, showing a difference of about 90 kW between the simulations. Since the ALM produces tip-vortices that cause losses, a tip-loss correction is not necessary if the tip vortices are well resolved.

3.6 Time-step

It is advised, by researchers in the field, to use a Δt, which allows the tip of the blade to not advance through more than one grid cell at each time-step. This condition is very restrictive because it requires a time-step smaller than what would be required by the more conventional Courant-Friedrichs-Lewy (CFL) condition. Figure 19 shows power output as a function of time-step for $\varepsilon = 8.4$ m. This shows a linear profile with a power variation ranging from 1 to 2%. This difference is small and does not suggest that the time-step is making a big difference in the simulation. Figure 20 shows mean velocity and vorticity contours for different time-steps. The profiles are very similar for all cases, suggesting that the time-step does not cause a significant difference. The value of $\varepsilon = 8.4$ used in this simulation is large. A smaller ε might produce different results because the tip vortices are more pronounced. As far as $\varepsilon = 8.4$ m, the time-step needs to not be limited by the tip speed.
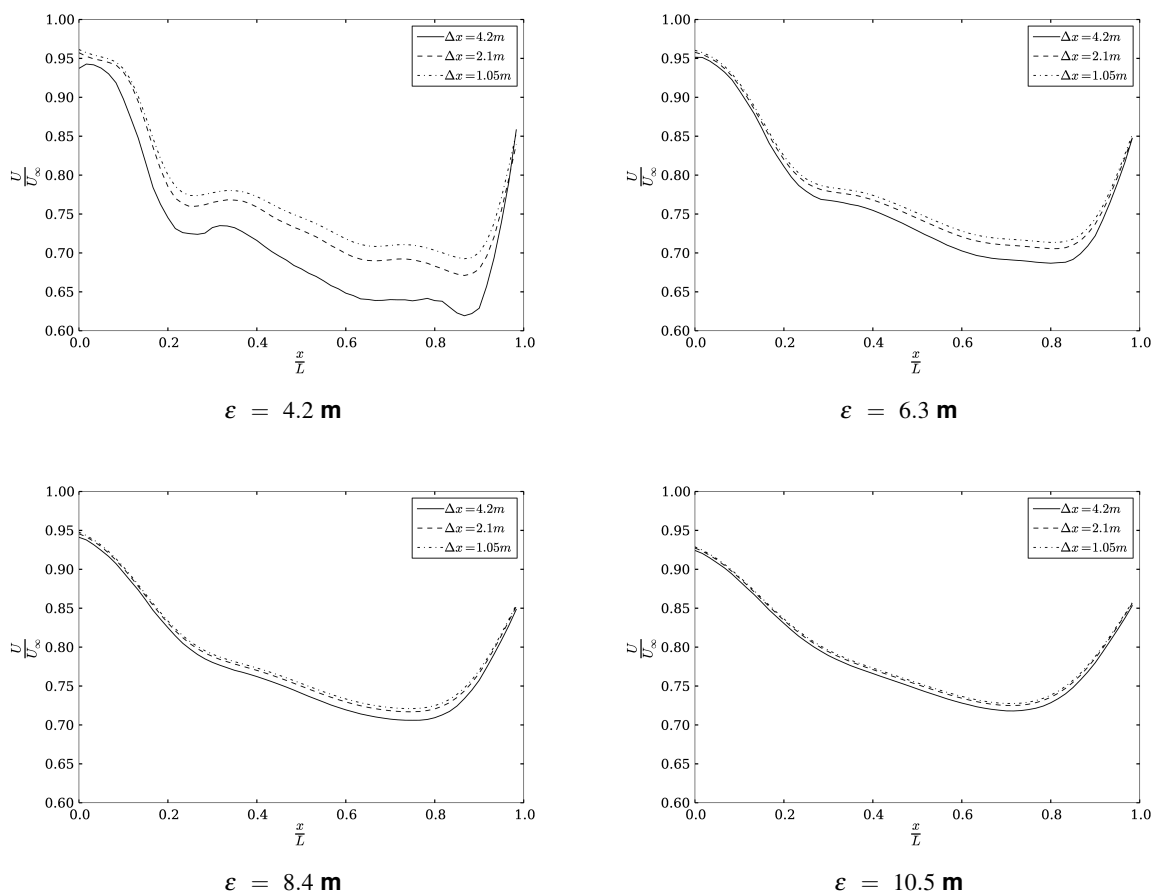
17

Figure 8. Axial velocity as a function of blade length for the ALM

3.7 Comparison

The ALM and ADM predict similar wake profiles and power output. The main differences between the models are: 1) the vortical structures near the rotor were captured by the ALM but not by the ADM, and 2) a non-symmetric wake was observed with respect to the center-line with the ALM, as opposed to the symmetric wake that was observed in the ADM. The ALM is able to capture vortical structures that are caused by the presence of individual blades. Tip and root vortices are captured when using the ALM with a high enough grid resolution, as seen in Figure 14, when $\varepsilon = 4.2$ m. However, the ADM does not allow these structures to form, only the shear layer of the wake forms.

Table 1 compares power output for the ADM, ALM, and BEM theory. A Richardson extrapolation is used to eliminate the leading error and predict the grid-converged power solution for the ADM and ALM. The power has a similar behavior for the ADM and ALM. As ε becomes smaller, the power output for the ADM and ALM approaches what the BEM theory predicts. Both models provide similar results, but as ε becomes smaller, the differences are bigger.

In terms of computational costs, the ALM needs to rotate the blades every time-step, and thus, apply forces at different finite-volume cells every time-step. A search for these cells is performed every time-step. The ADM points are fixed and do not rotate every time-step. All the cells that lie adjacent to the disk are assigned at the beginning of the simulation, thus all the finite-volume cells that have an applied force are searched for only once. The ADM, by

18

ALM   ADM

$\varepsilon = 4.2$ m

$\varepsilon = 6.3$ m

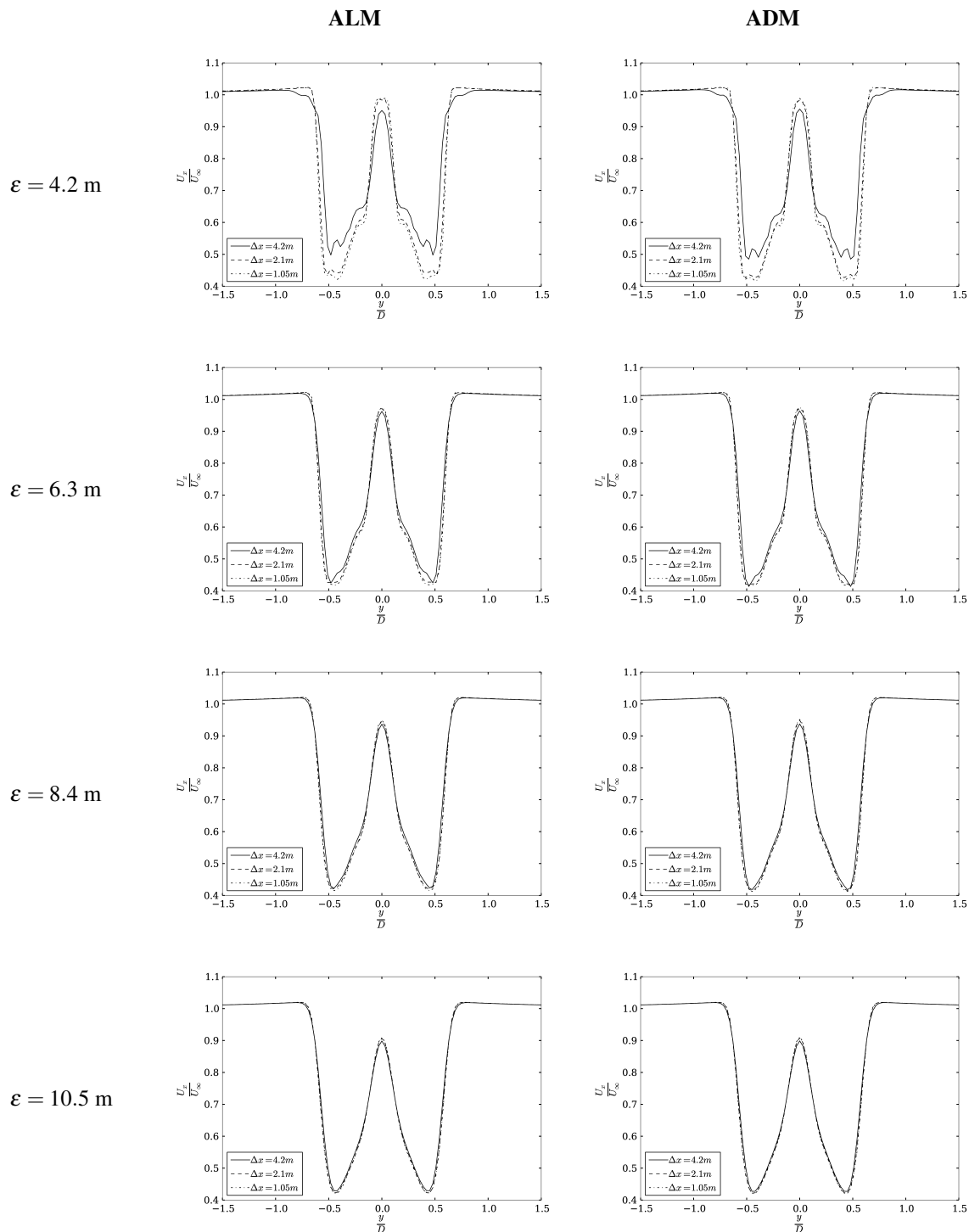$\varepsilon = 8.4$ m

$\varepsilon = 10.5$ m

Figure 9. Mean velocity in the cross-stream direction that is 1 diameter behind the turbine rotor are shown, as predicted by the ALM (left column) and ADM (right column). Each row shows plots that are the result of using different values of the body force projection width (ε).
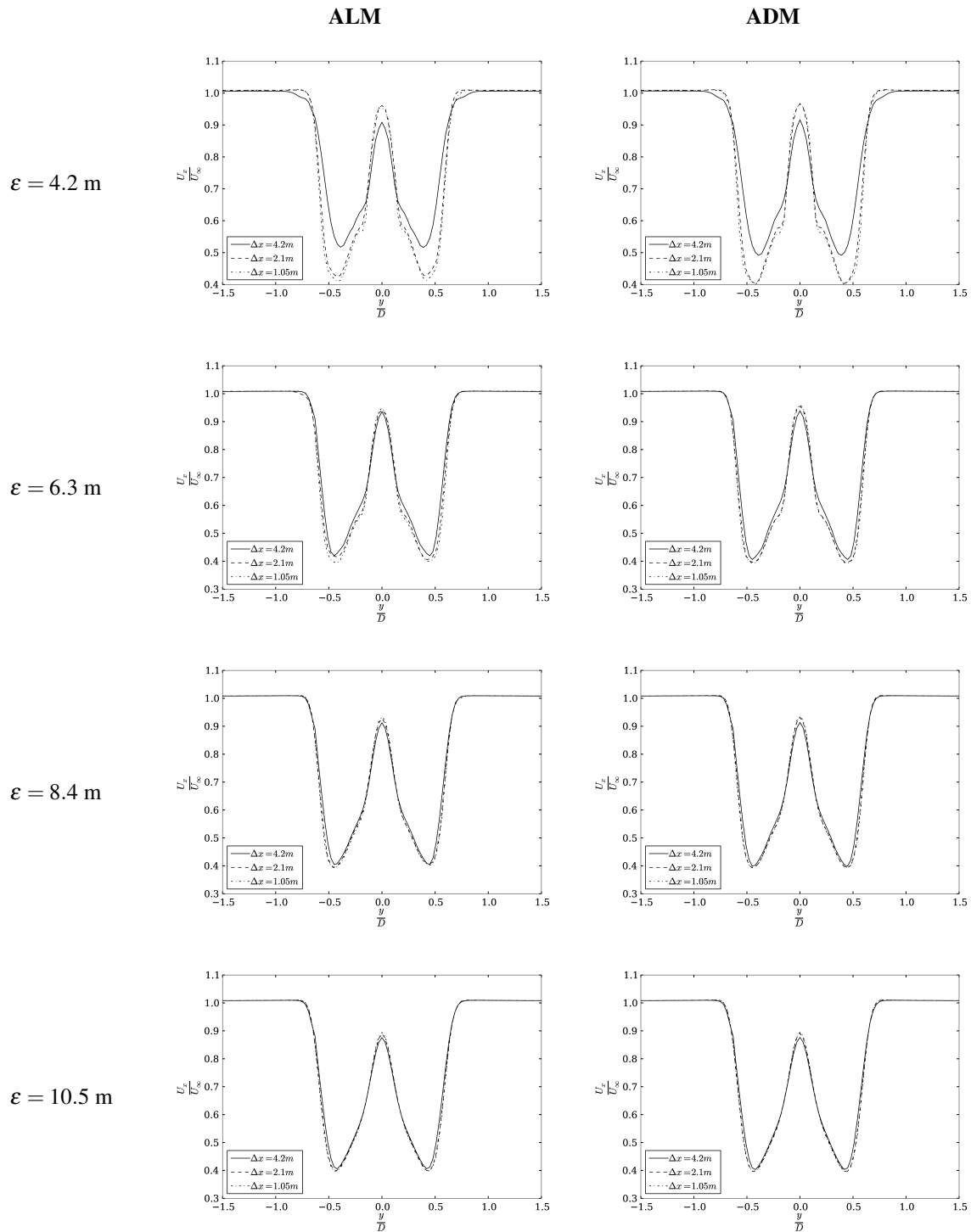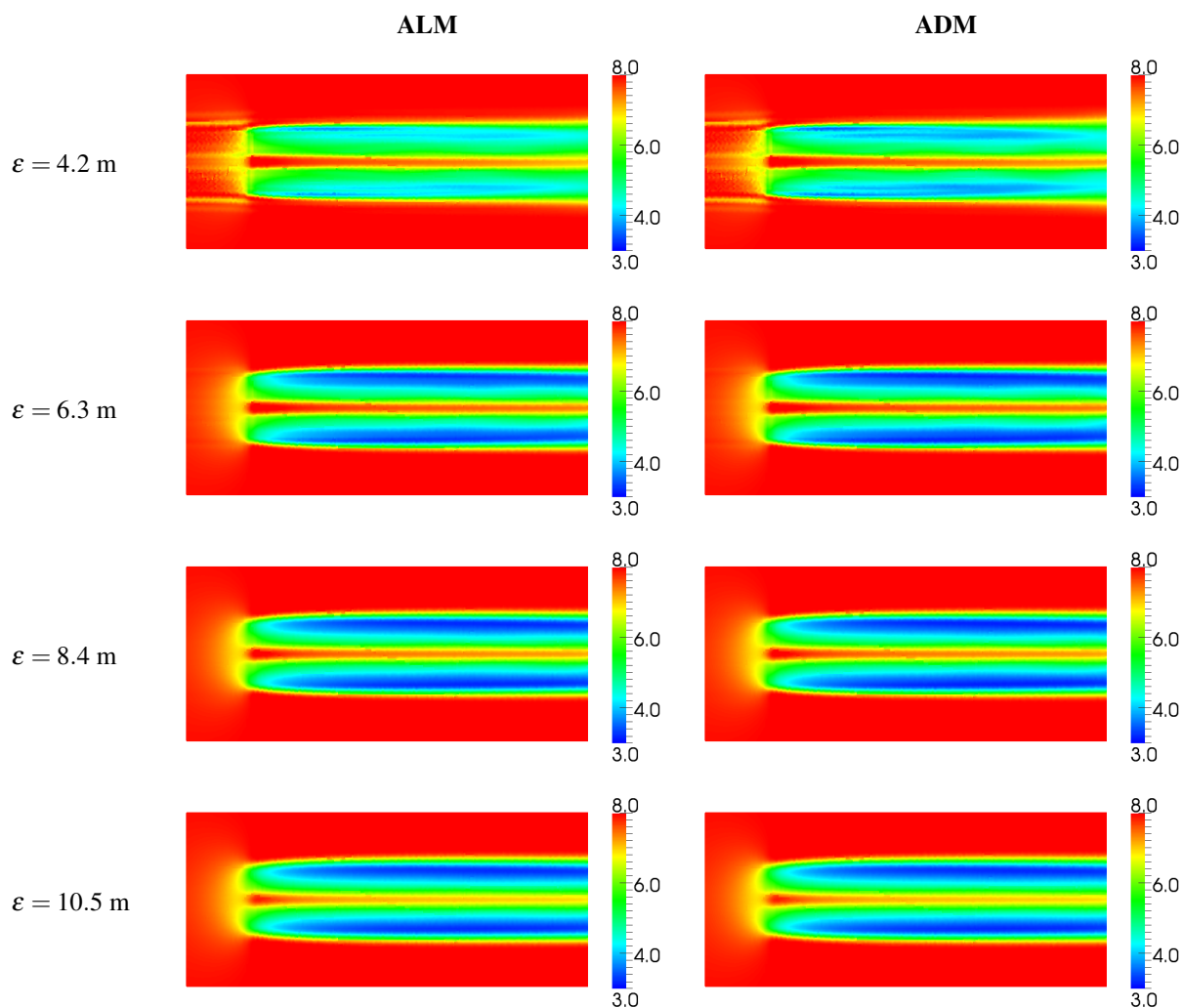
19

ALM   **ADM**

$\varepsilon = 4.2$ m

$\varepsilon = 6.3$ m

$\varepsilon = 8.4$ m

$\varepsilon = 10.5$ m

Figure 10. Mean velocity in the cross-stream direction that is 4 diameters behind the turbine rotor are shown, as predicted by the ALM (left column) and ADM (right column). Each row shows plots that are the result of using different values of the body force projection width (ε).

20

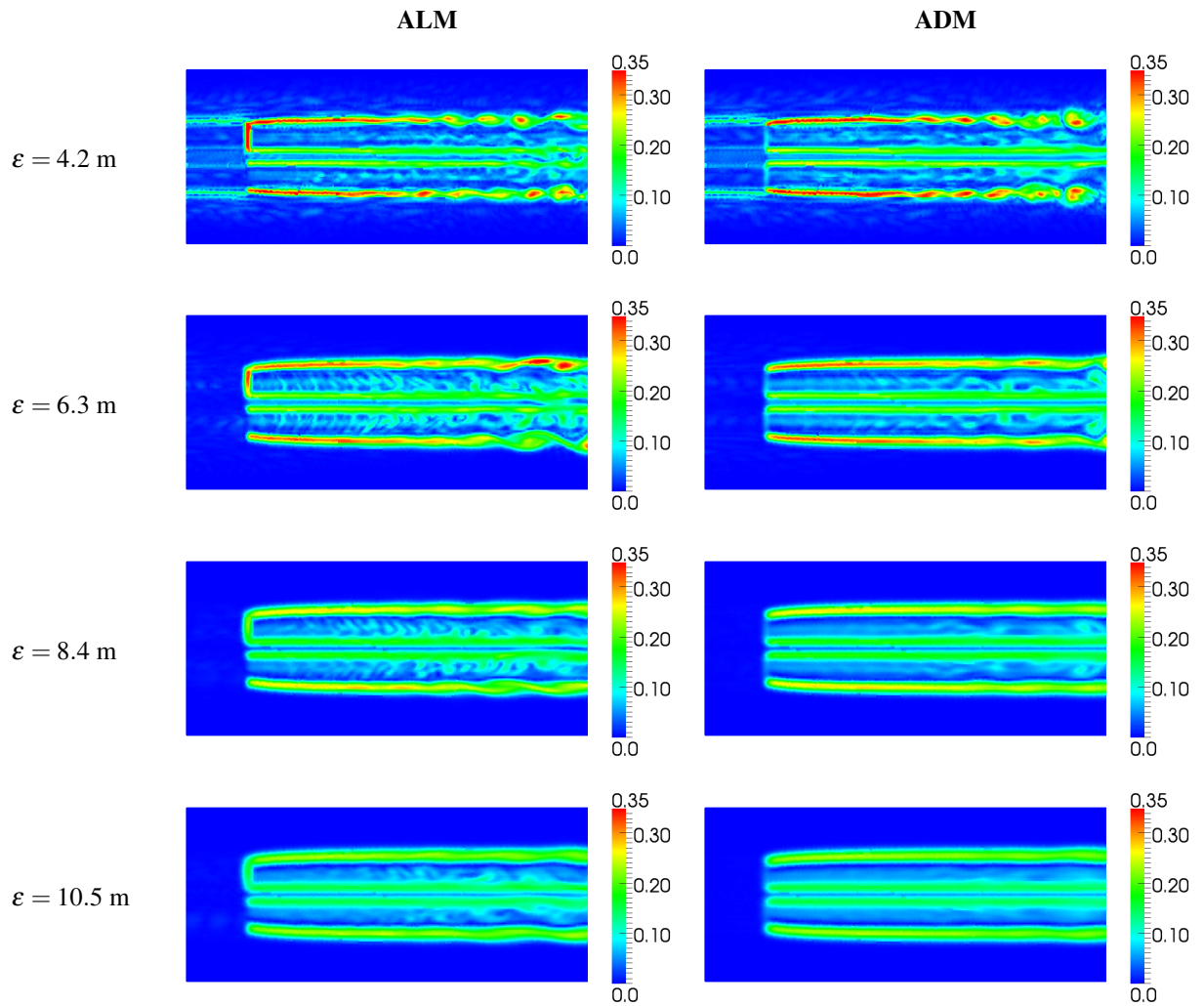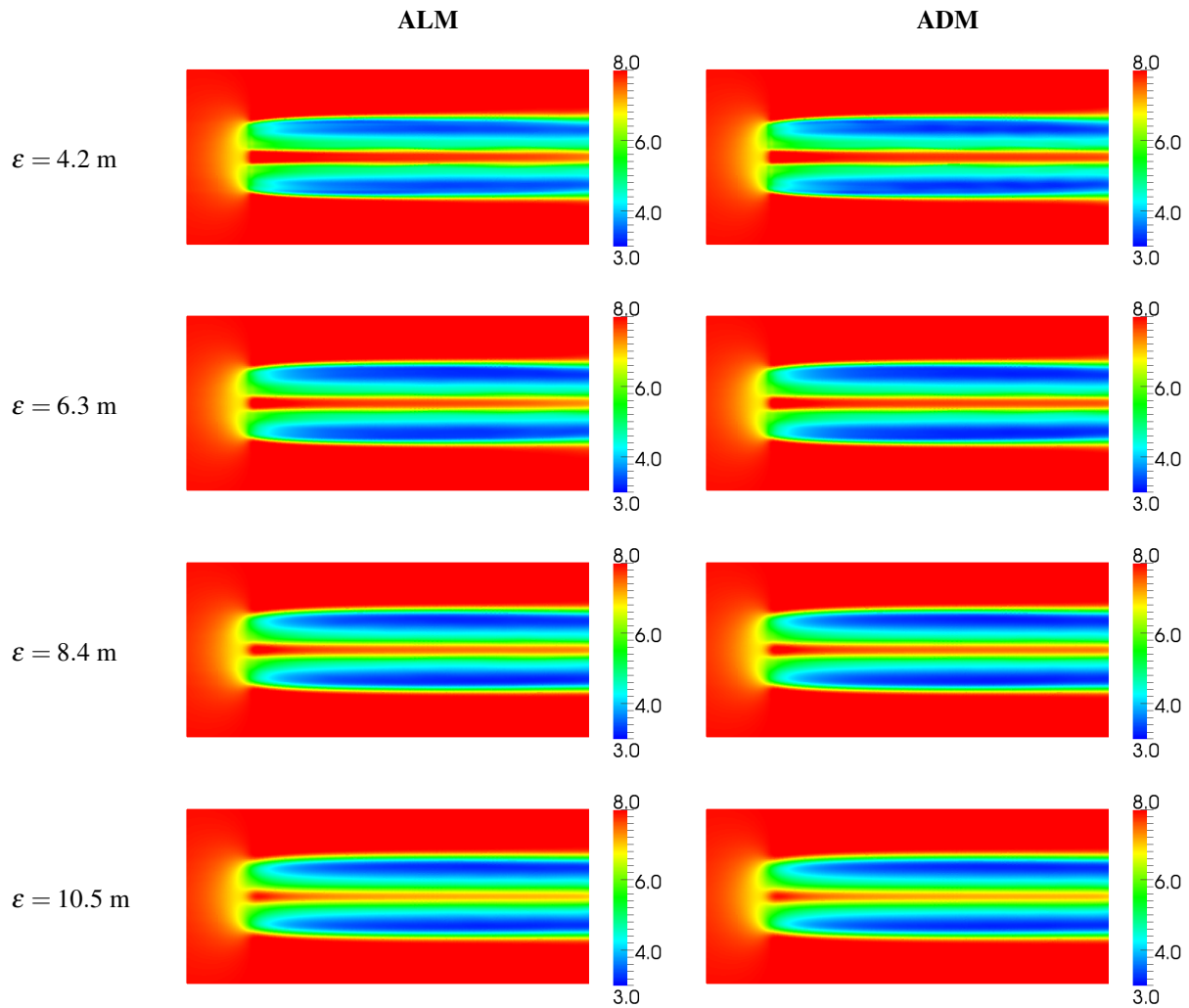**Figure 11. Mean velocity (m/s) contours in a plane through the turbine hub are shown, as predicted by the ALM (left column) and ADM (right column), with a mesh resolution of $\Delta x = 4.2$ m. Each row shows contours that are the result of using different values of the body force projection width (ε).**

Table 1. Percentage difference between the ADM, ALM, and BEM theory in terms of power production. A Richardson extrapolation is used to approximate the converged solution for the ALM and ADM.

| Case	Predicted Power (MW)		Percentage Difference with BEM	
	ALM	**ADM**	**ALM**	**ADM**
$\varepsilon = 2.1$ m	1.81		-6.0%	
$\varepsilon = 4.2$ m	2.13	2.14	10.6%	11.0%
$\varepsilon = 6.3$ m	2.19	2.19	13.7%	13.7%
$\varepsilon = 8.4$ m	2.23	2.23	15.7%	15.7%
$\varepsilon = 10.5$ m	2.27	2.27	17.9%	17.9%

21

Figure 12. Vorticity magnitude (1/s) contours in a plane through the turbine hub are shown, as predicted by the ALM (left column) and ADM (right column), with a mesh resolution of $\Delta x = 4.2$ m. Each row shows contours that are the result of using different values of the body force projection width (ε).
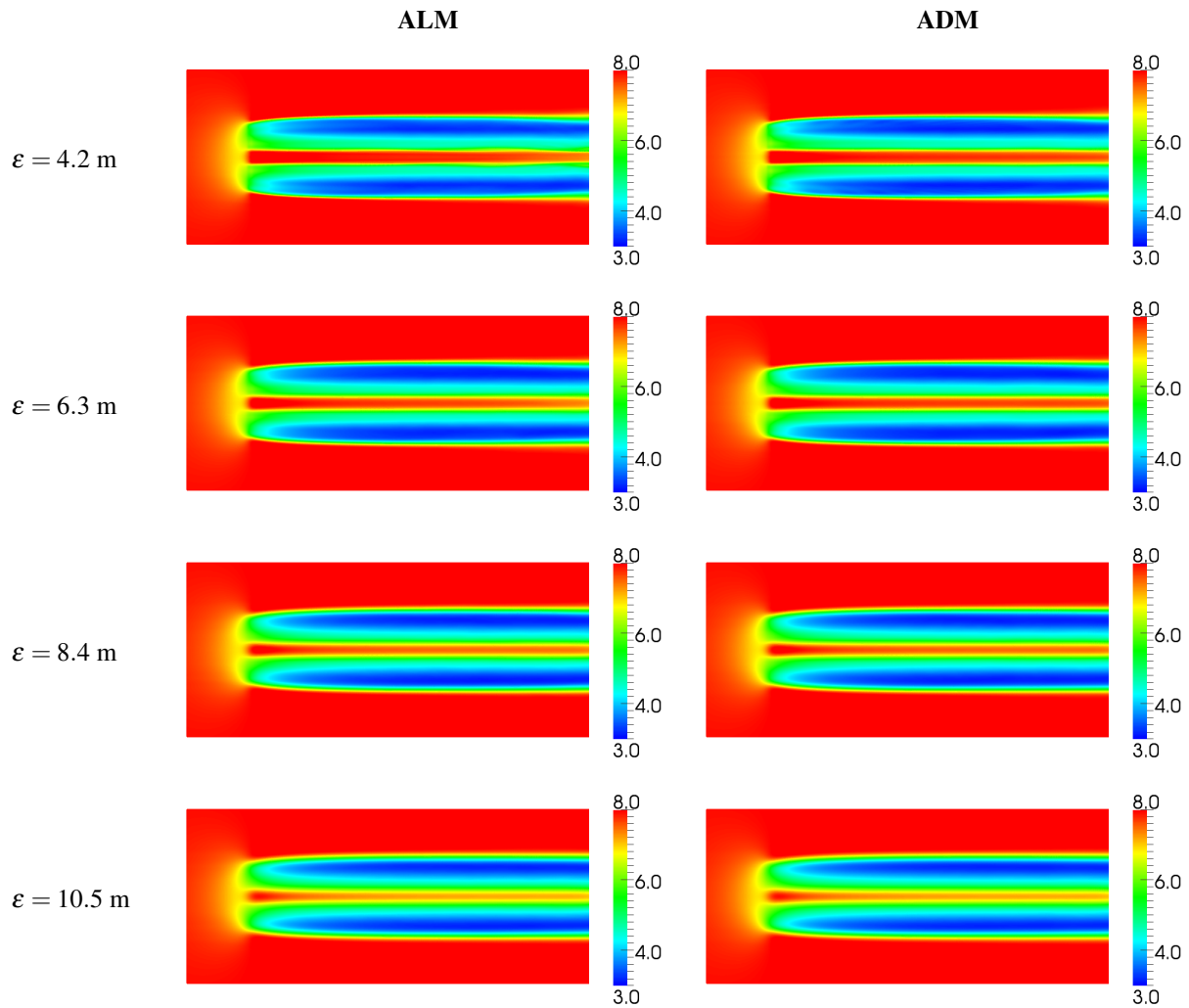
22

Figure 13. Mean velocity (m/s) contours in a plane through the turbine hub are shown, as predicted by the ALM (left column) and ADM (right column), with a mesh resolution of $\Delta x = 2.1$ m. Each row shows contours that are the result of using different values of the body force projection width (ε).
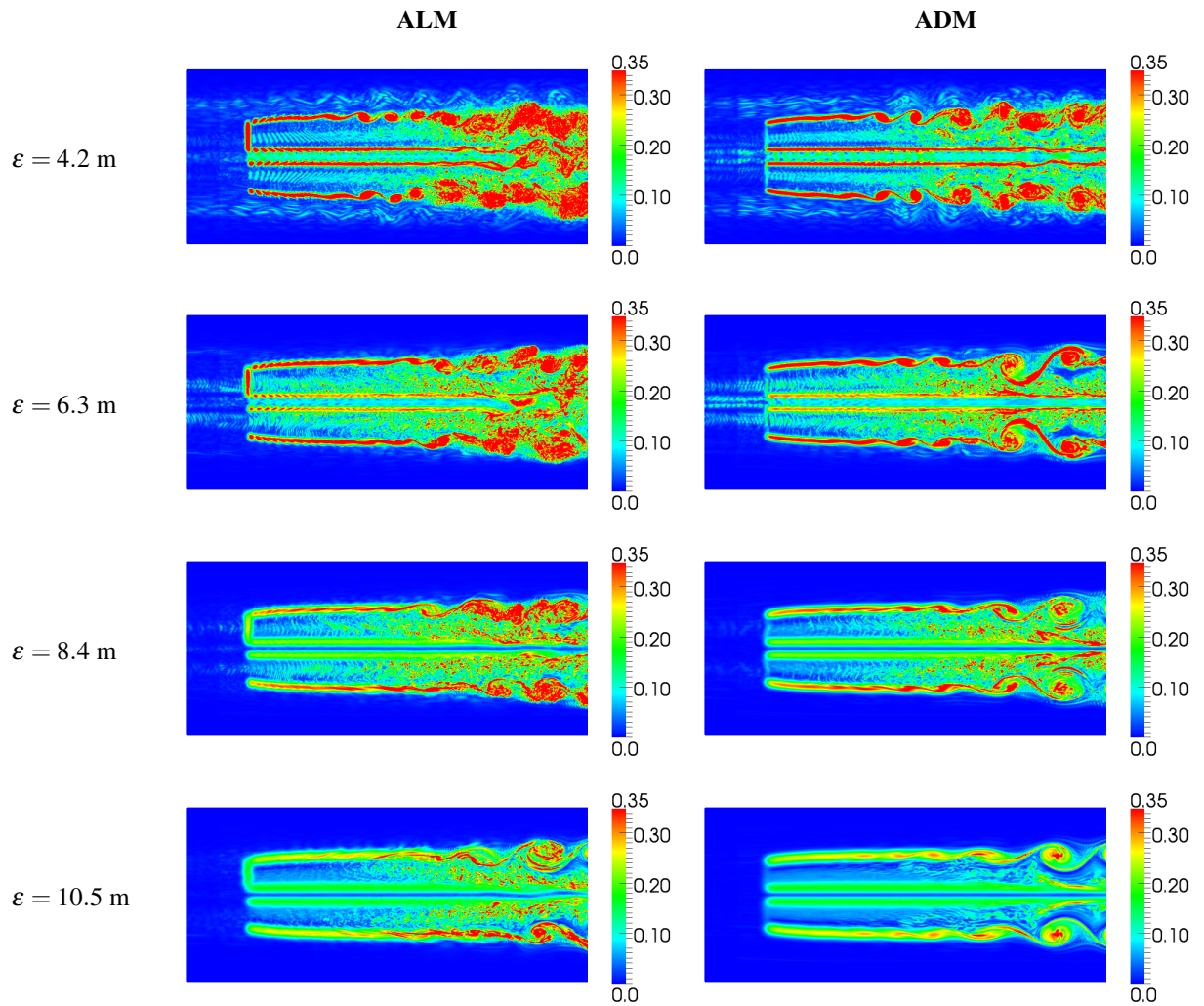
23
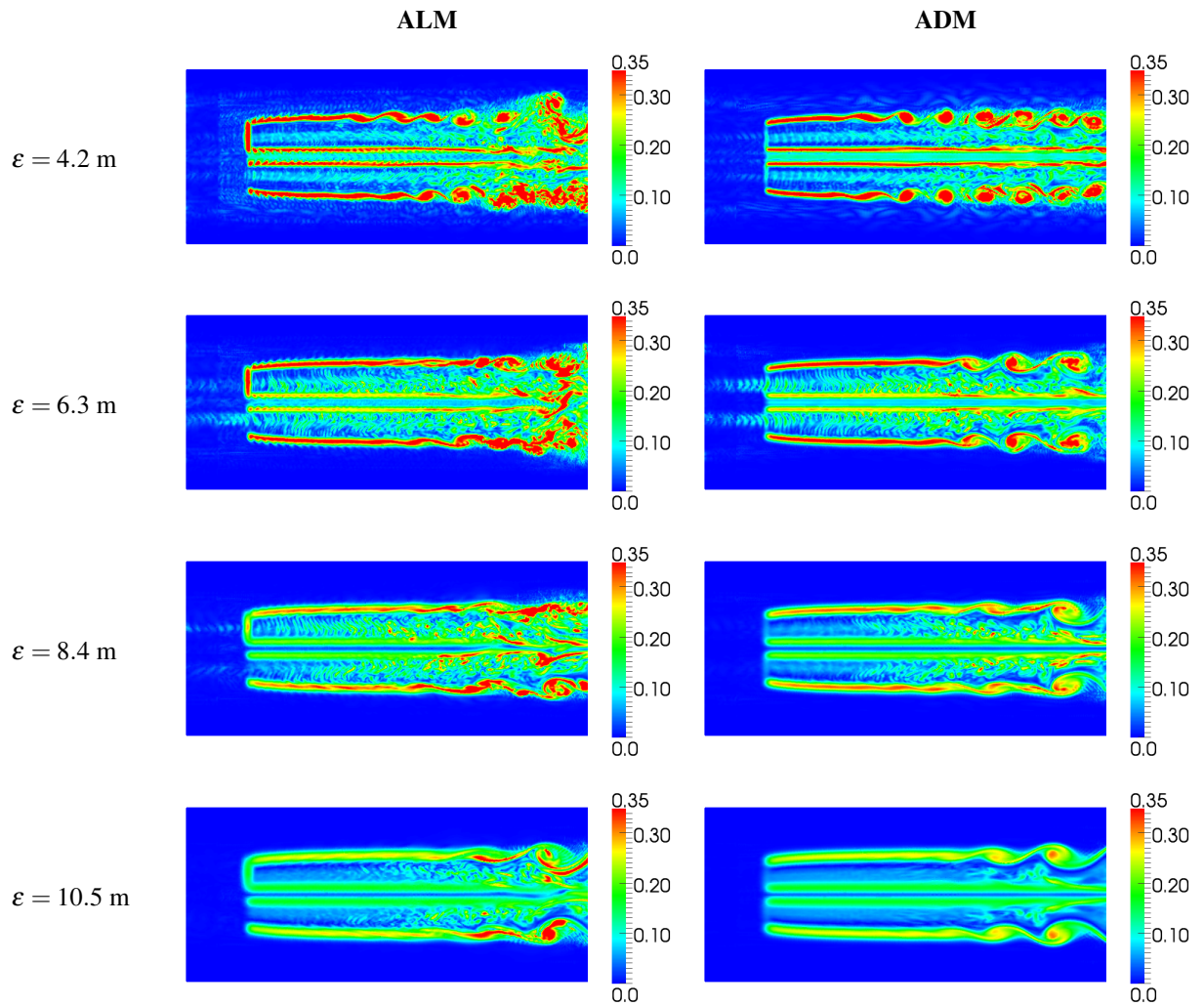
Figure 14. Vorticity magnitude (1/s) contours in a plane through the turbine hub are shown, as predicted by the ALM (left column) and ADM (right column), with a mesh resolution of $\Delta x = 2.1$ m. Each row shows contours that are the result of using different values of the body force projection width (ε).

24

ALM

ADM

$\varepsilon = 4.2$ m

$\varepsilon = 6.3$ m

$\varepsilon = 8.4$ m

$\varepsilon = 10.5$ m

Figure 15. Mean velocity (m/s) contours in a plane through the turbine hub are shown, as predicted by the ALM (left column) and ADM (right column), with a mesh resolution of $\Delta x = 1.05$ m. Each row shows contours that are the result of using different values of the body force projection width (ε).
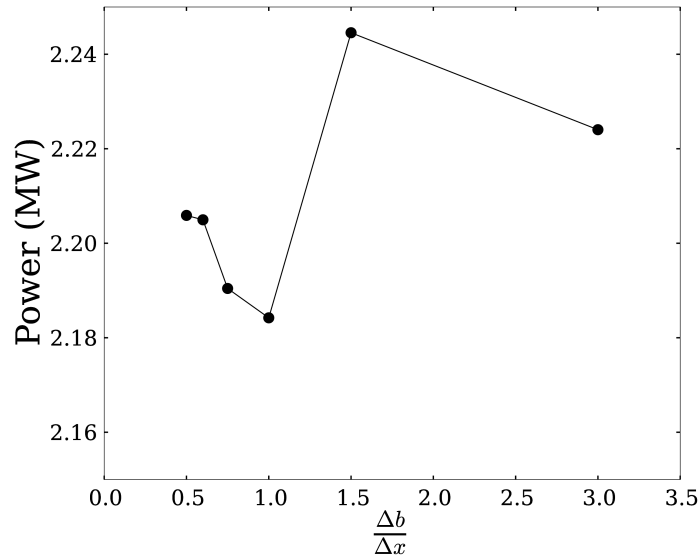
Figure 16. Vorticity magnitude (1/s) contours in a plane through the turbine hub are shown, as predicted by the ALM (left column) and ADM (right column), with a mesh resolution of $\Delta x = 1.05$ m. Each row shows contours that are the result of using different values of the body force projection width (ε).

Figure 17. Power output for the ALM as a function of actuator point resolution along the blade, with $\varepsilon = 8.4$ and a grid resolution of 2.1 m
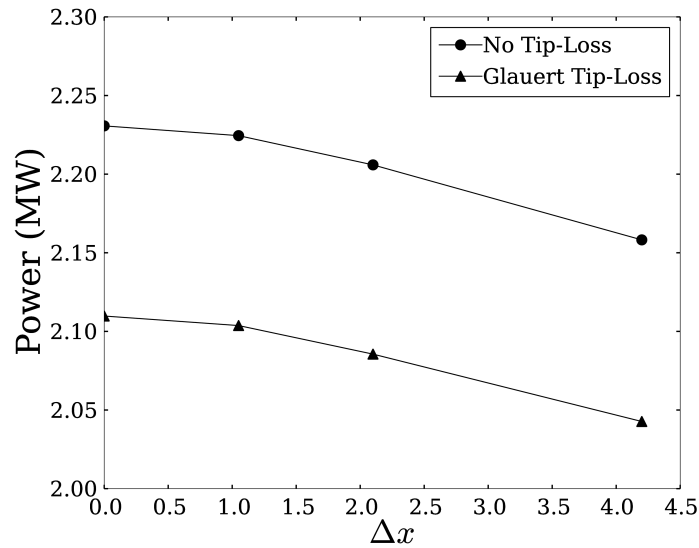

Figure 18. Power output as a function of grid resolution for $\varepsilon = 8.4$ m, with and without a tip- and root-loss correction for the ALM

contrast, has more points than the ALM and the forces on these points must be calculated for every time-step. These differences do not impact the simulation time significantly. However, time-step size will have a significant impact on simulation time. The time-step for simulations performed using the ALM is restricted by the tip speed. The tip
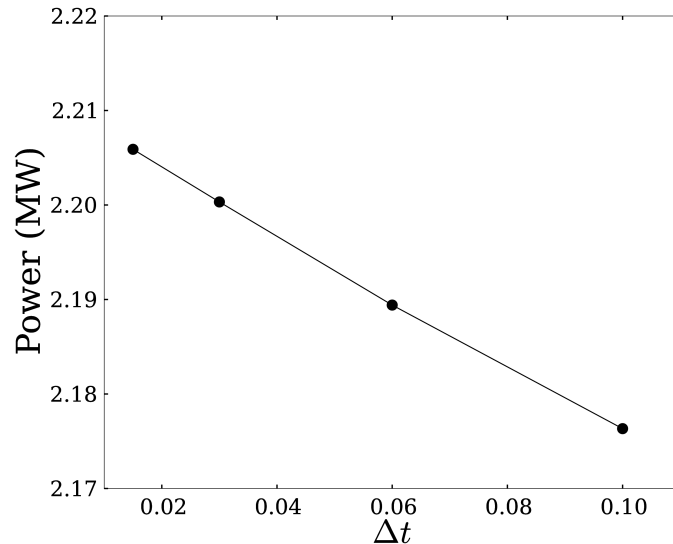
27

Figure 19. Power output as a function of time-step for $\varepsilon = 8.4$ m

of the blade should not pass through more than a single finite-volume cell each time-step. This condition is far more restrictive than the typical CFL condition. For a case with λ=8, the time-step needs to be eight times smaller using this restriction than with the CFL condition. Resolving the root- and tip-vortices compromises the simulation time-step and thus increases computational cost. The ADM will provide an accurate solution with a time-step that is based on a CFL condition, rather than on tip speed. If the simulations require solving the flow structures near the rotor, the ALM should be used. For simulations related to the far wake, the ADM will provide a reasonable solution without compromising the simulation time-step.

3.8 The ε Parameter

A Gaussian function is introduced to turn the set of unphysical point forces into a continuous volume force field. The use of a Gaussian function avoids numerical instabilities caused by the application of forces on discrete sections of the blade. The width of the function is determined by the ε parameter. This parameter plays an important role in the models studied. We found that a parameter closest to the characteristic length of the blade section under study yielded the best results. The value of the Gaussian function decays to 1% of its initial value at a distance of $r = 2.15\varepsilon$. To span the force of a blade section through the area that covers the distance from the leading edge to the trailing edge, a value of $\varepsilon = c/4.3$ would be required. With a chord value around 4 m for the NREL 5-MW turbine, a value of $\varepsilon = 4\,\text{m}/4.3 = 0.93$ m creates numerical instabilities on the grids used in this study. Our projections show that making the grid smaller would be expensive unless a fine grid local to the rotor was used.

The simulations presented show that as ε becomes smaller, the power decreases. Note that a small value of ε relative to the grid size produces numerical instabilities in the solver. These instabilities affect the solution and can be observed in the wake profiles and angle of attack for a case in which $\varepsilon = 4.2$ m and a grid resolution of 4.2 m. When parameter ε was the same size as the grid size ($\varepsilon/\Delta x = 1$), the simulations for the ALM and ADM became unstable. This can be avoided by choosing a value of $\varepsilon/\Delta x > 2$, as suggested by Troldborg [9]. There is an optimum point for the Gaussian width to match what the BEM theory predicts. This optimum is related to the geometry of the blade. In this case, the solution given by the BEM theory lies somewhere between $\varepsilon = 4.2$ and 2.1 m. It is unclear which value of ε matches the geometry of the blade section and would accurately predict power using the ALM. The results
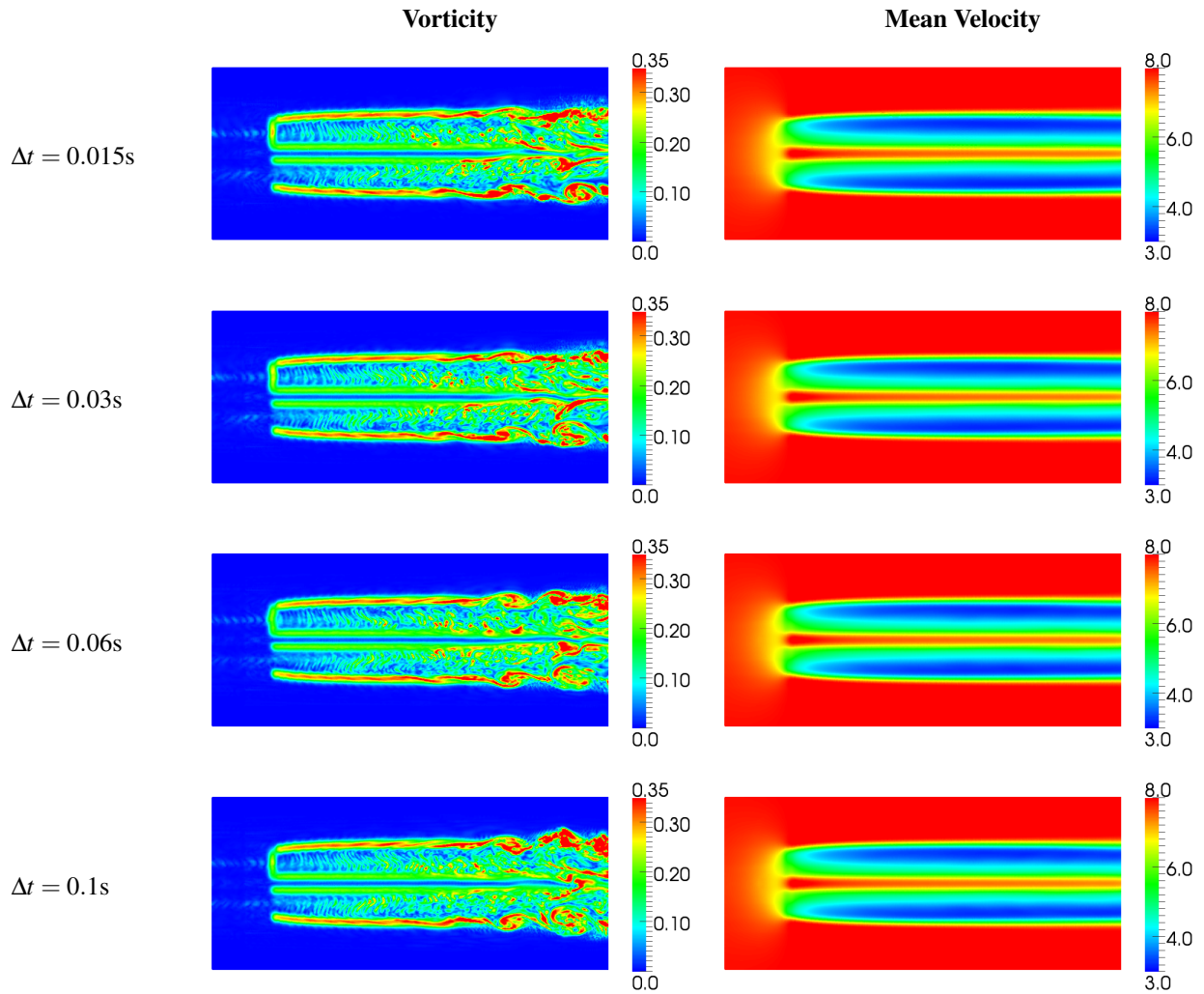
28

Figure 20. Mean velocity (m/s) and vorticity magnitude (1/s) contours in a plane through the turbine hub for $\varepsilon = 8.4$ m are shown. Each row shows contours that are the result of using different time-step values.

suggest that the value of ε should not be fixed to a value that satisfies the condition that $\varepsilon = c/4.3$. A condition that better approximates the physical force distribution of an airfoil should be used, varying ε along the span as the chord varies.

Increasing the value of ε thickens the shear layer surrounding the wake. As the shear layer is thickened, there is less vorticity in the flow. This is illustrated in Figures 12, 14, and 16, as the vorticity decreases with larger ε.

4 Wind Tunnel Simulations

We have performed a validation of the actuator line model (ALM) that compares the numerical results with the experiments done at the low-speed closed-return wind tunnel at the Department of Energy and Process Engineering at the Norwegian University of Science and Technology, Trondheim [26][27]. The tunnel has a test section of 1.85 meters (m) (height) $\times$ 2.71 m (width) $\times$ 11.15 m (length). The test section height is adjustable to account for wall boundary layer growth. In this study, we aimed to numerically simulate the experimental setup.

We performed simulations for tip speed ratios (λ) of 3, 4, 6, 9, and 12 and compared the power and thrust coefficients against the experimental data. In addition, we used wake visualizations to illustrate the difference in the breakdown of the wake for different tip speed ratios as well as sampled wake profiles.

4.1 Turbine Model

The turbine modeled has a rotor with a diameter of 0.894 m and a tower with a height of 0.817 m. The blades use the National Renewable Energy Laboratory (NREL) S826 airfoil along the entire span. We obtained two-dimensional lift and drag coefficients from the NREL S826 report [28] and corrected for stall delay using NREL's AirfoilPrep tool [29]. The actuator line model accounts for only the blades of the turbine and does not include the hub, tower, or nacelle. The turbine is located 3.66 m from the tunnel inlet and is laterally centered.

4.2 Mesh

The mesh of the tunnel consists of a block with dimensions (11.15 m $\times$ 1.851 m $\times$ 2.71 m). The walls are refined in an attempt to capture the boundary layer. The height of the tunnel varies linearly along the streamwise direction from 1.801 m to 1.851 m. The mesh is refined near the walls to capture the boundary layer. The walls have a no-slip condition. The grid resolution near the wall does not resolve the boundary layer completely, but because the rotor is far from the walls, we believe the effect of not resolving this boundary layer is negligible. The mesh is locally refined near the rotor with $\Delta x/D = 0.006$. This refinement allows the simulation to calculate power production accurately (following the results from the previous section).

The boundary layer is measured to be 0.1 m at the tunnel inlet. The inlet bulk velocity is taken to be 10 meters per second (m/s). The inlet boundary condition is set to match the turbulent boundary layer profile using

$$U = \left(\frac{y}{\delta}\right)^{1/7} \tag{4.1}$$

At $y > \delta$, the velocity is set to 10 m/s with no turbulence.

4.3 Results

Power and thrust coefficients are shown as a function of tip speed ratio in Figure 21. The maximum power coefficient of 0.47 is at a tip speed ratio of 6. This corresponds to the highest induction factor, as we expected. For the case with lowest tip speed ratio, the simulation power coefficient lies on top of the experimental data. Thrust coefficient is under-predicted for all tip speed ratios.

Figure 22 shows wake profiles in the spanwise direction for 1, 2, 3, and 4 diameters behind the rotor. The profiles show how the wake deficit is stronger for higher tip speed ratios. Note that for stronger wake deficits, the velocity near the edges and in the center of the rotor is larger, because of mass conservation. Figure 23 shows wake profiles for cases with tip speed ratios of 3 and 6 that are one diameter behind the rotor. The wakes in the simulation are different from the experimental data at the center. This difference is because the nacelle is not a part of the model. It is clear that the nacelle needs to be incorporated into the model to obtain accurate wake profiles. As a result, this

difference causes the thrust to be lower than expected, because the nacelle will contribute a drag force to the model. For this reason, the thrust coefficient curve for the simulations lies below the experimental data. Away from the center, the wake profiles agree with the experimental data.

Figure 24 shows a rendering of the Q-criterion [30] for tip speed ratios of $\lambda = 3, 6, 9,$ and 12. The Q-criterion is the second invariant of the velocity gradient tensor. Where it is positive, it shows regions of the flow where rotation dominates strain, and where it is negative, strain dominates rotation. This illustrates that the breakdown of the wake is faster with increased tip speed ratio. With higher tip speed ratio, the wake deficit is greater, as shown in Figure 22, indicating there is a stronger, more unstable wake-edge shear layer. This causes faster transition to turbulence and faster wake breakdown. The visualizations show that at higher tip speeds, the wake starts interacting with the tunnel walls. This interaction affects the wake, as it is not able to fully expand.

The ALM is a good representation of the turbine in the tunnel, but is missing some key elements in its implementation. The model is able to capture the blades inside the flow field. Because the power of the turbine is being extracted by the blades, the power coefficient is close to what experiments predict. However, the effect of the nacelle is not included in the model. The nacelle contributes to the thrust experienced by the turbine, and, for this reason, the thrust coefficient is under-predicted by the model. Tip speed ratio affects the power produced by the turbine and the structure of the wake. The maximum power coefficient is reached at a tip speed ratio of 6, which approximates the Betz limit. A faster tip speed ratio causes a faster breakdown of the wake.
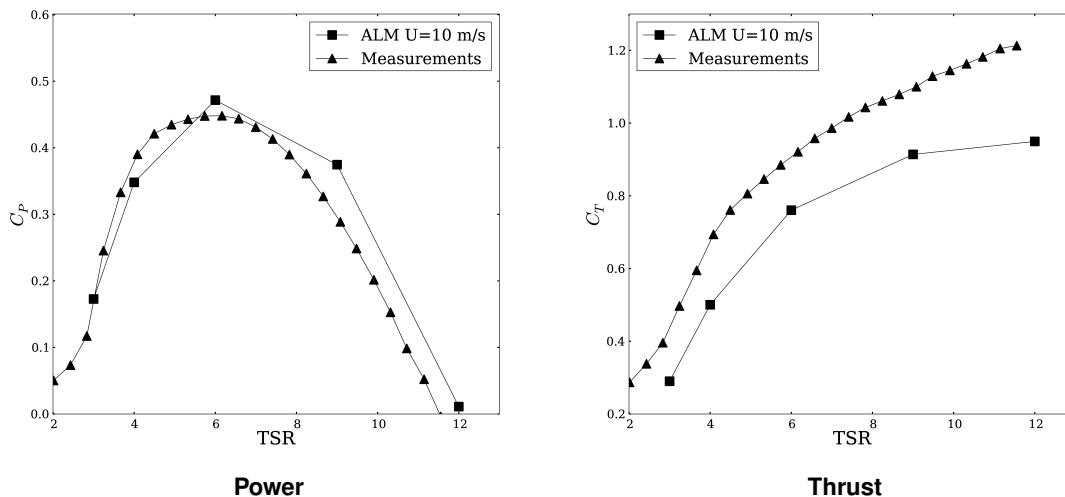

Power **Thrust**

Figure 21. Power and thrust coefficients as a function of tip speed ratio

$x/D \; = \; 1$

$x/D \; = \; 2$

$x/D \; = \; 3$

$x/D \; = \; 4$
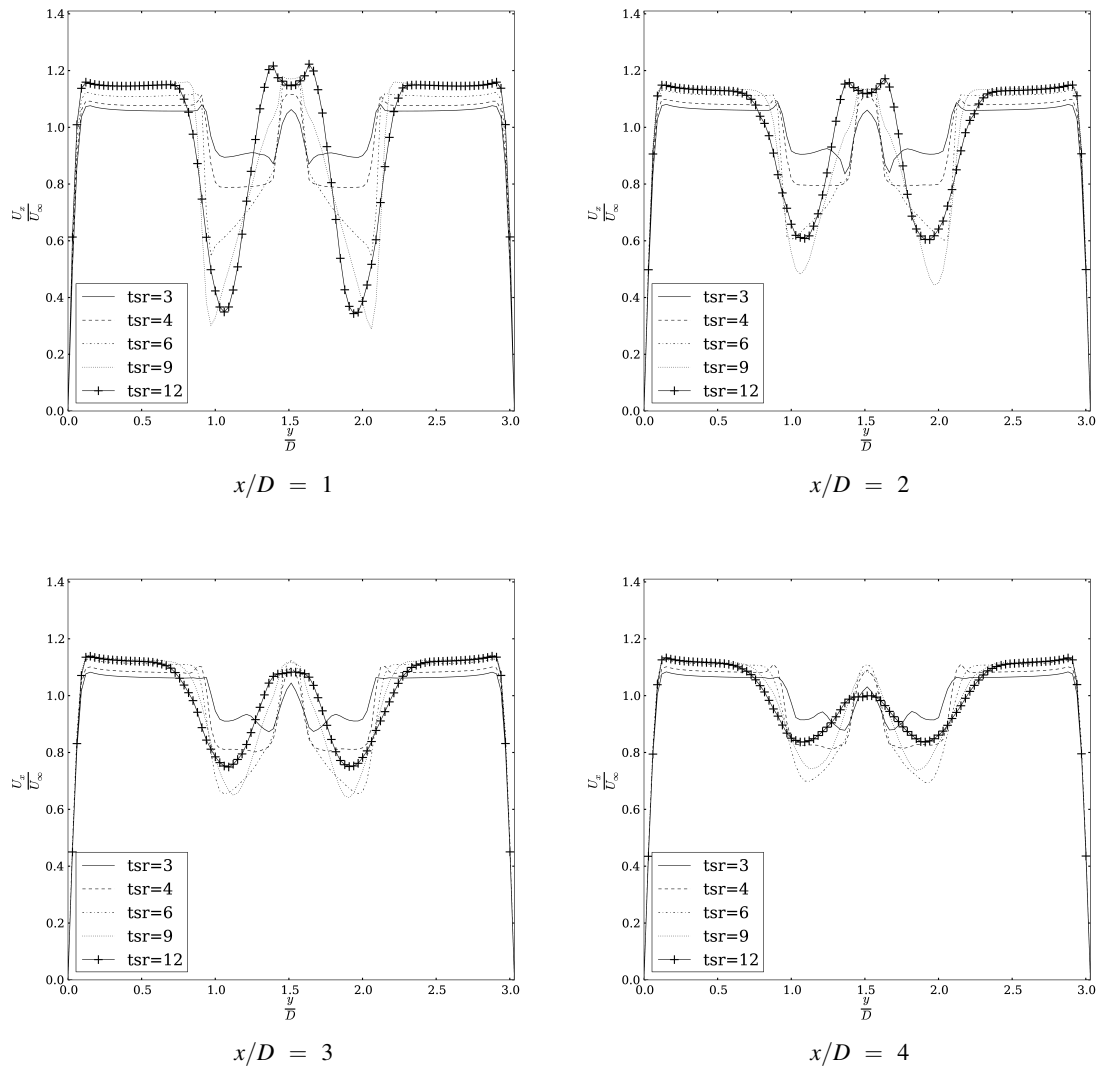
Figure 22. Mean velocity profiles behind the rotor

33

1D, TSR=3

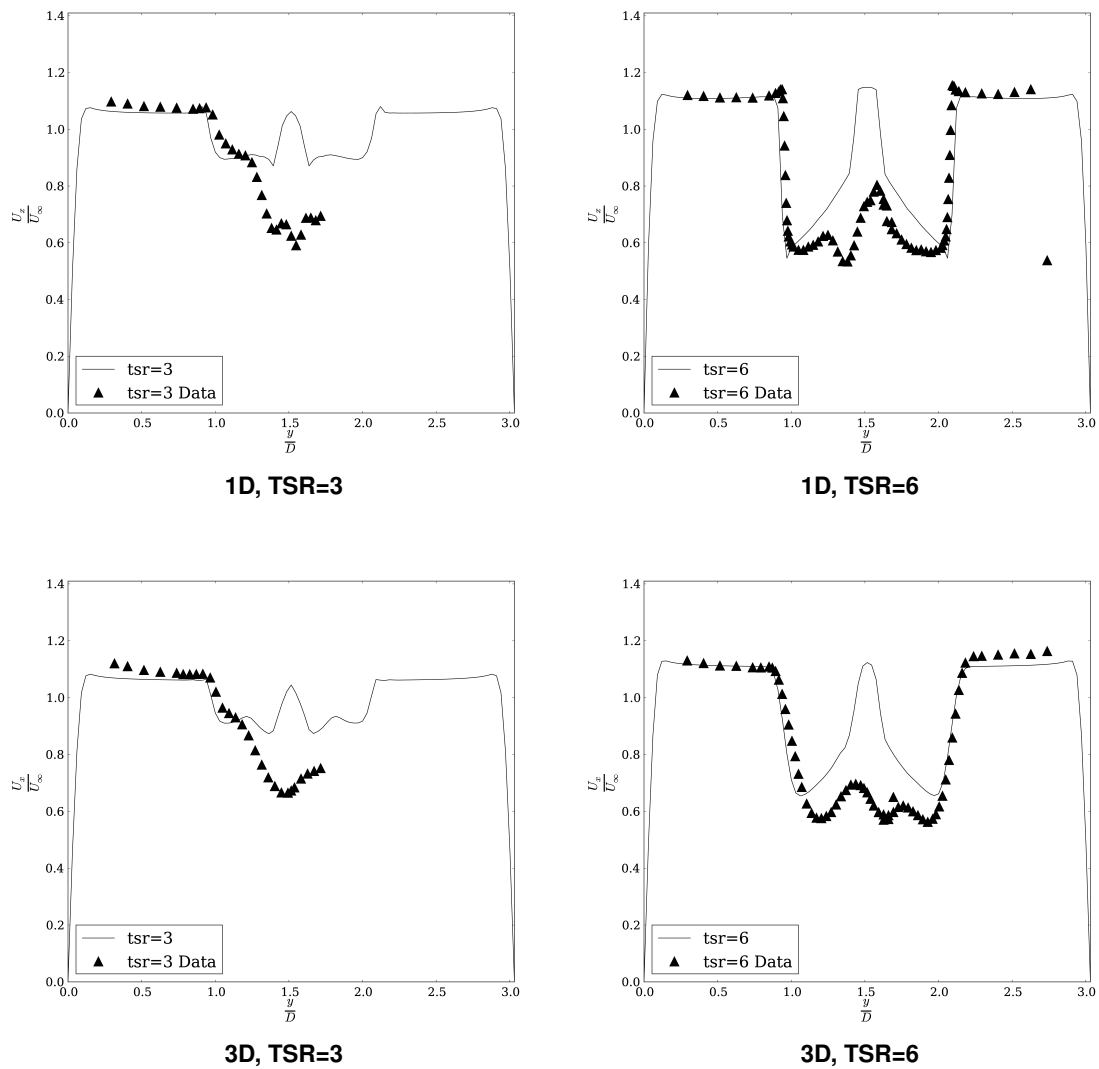**1D, TSR=6**

3D, TSR=3

3D, TSR=6

Figure 23. Mean velocity profiles one and three diameters behind the rotor
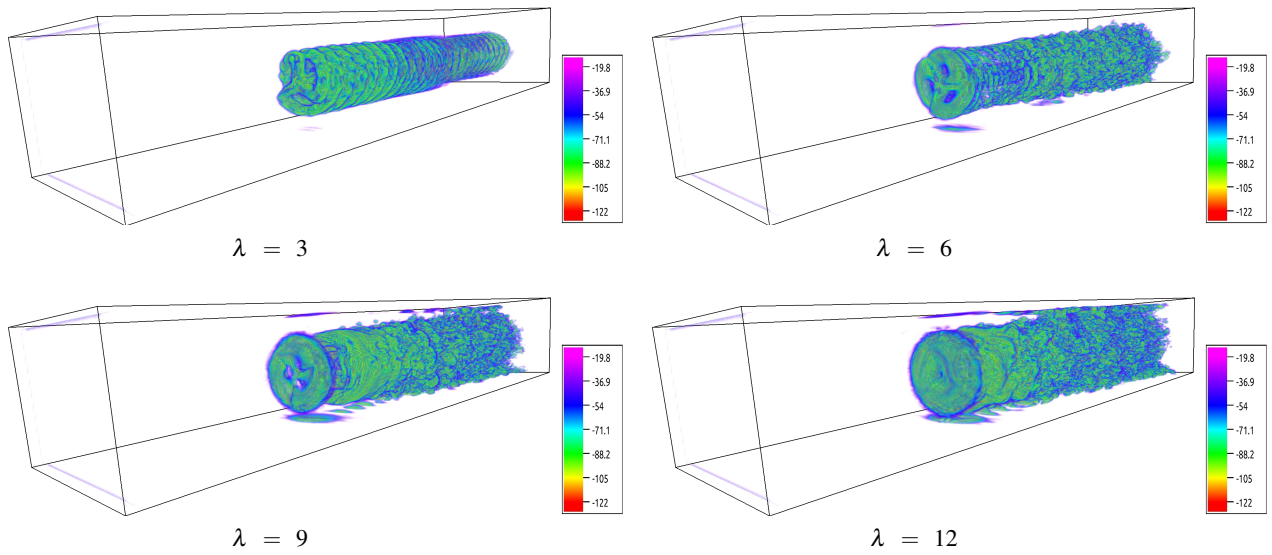
34

Figure 24. Q-criterion ($1/s^2$) rendering showing the structure of the wake for different tip speed ratios

5   Wind Farm Simulation

5.1   Introduction

This section presents the results of a large-eddy simulation (LES) of the flow of over 48 multi-megawatt turbines that compose the Lillgrund wind plant. We compared the performance of the actuator line (ALM) and actuator disk model (ADM) in wind farm simulations. Churchfield et al. [31] performed an LES of the Lillgrund wind farm using the ALM; we performed the same simulation using the ADM and compared the results for both models. The simulated wind farm is the Lillgrund offshore facility operated by Vattenfall Vindkraft AB. Lillgrund is located 7 kilometers (km) off the coast of Sweden and 7 km south of the Öresund bridge. Figure 25 shows the turbine siting and the computational domain. Positive x and y correspond to east and north, respectively.

We used LES to simulate the atmospheric boundary layer (ABL) with the standard Smagorinsky model. We modeled the sea surface as a rough, flat surface with an aerodynamic roughness height of 0.1 millimeters (mm), which was appropriate for the sea surface. The turbine model operating at the Lillgrund facility is the Siemens SWT-2.3-93. The turbine model was provided by Churchfield, who reverse-engineered the available turbine information [32]. We performed the simulation in two steps: running an ABL precursor simulation and running the wind plant simulation. The first precursor simulation tried to match the Lillgrund wind conditions as closely as possible and was obtained from Churchfield [31]. We chose a mean velocity of 9 m/s at hub-height with a wind direction of 221.6^o. At these conditions, the turbines operating in Region 2, wake deficits are the strongest. We used the turbulent intensity at hub-height of 6.2%, which is typical at the chosen wind direction. The precursor simulation was used to create a turbulent wind inlet (west and south) boundary condition on velocity and temperature for the simulation. The east and north planes were set to zero gradient for velocity and temperature. The velocity top boundary condition was set to zero in the normal direction and to zero gradient in the other two directions. The pressure boundary conditions were set to hydrostatic gradient on the top and bottom and to zero gradient on the sides. The temperature gradient on the top was set to 0.003 Kelvins per meter (K/m) to follow the temperature profile in capping inversion. The precursor simulation was the same for both the ADM and ALM simulation. The time-step of the ALM simulation was fixed at the condition that the tip of the blade should not go through more than one grid cell at each time-step. The time-step in the ADM simulation was based on the maximum Courant number not exceeding a limit of 0.75. The wind plant simulation was for 10 minutes of real time and an initial transient of 150 s.

5.2   Results

Normalized power output is shown for all the rows in the turbine array in Figure 26. Rows B through D are compared against field data that were averaged over a year and binned by wind direction. Power output for these rows is normalized using the average power of the first turbine in rows B, C, and D. The other turbines are normalized using the power of the first turbine in their row. The simulations agree with field data. The largest difference is on the last turbines in the rows, where the simulation predicted an increase in power production. Figure 27 shows non-normalized power output for all the turbines. Power production for the ADM agrees well with that for ALM, although we observe slight differences. The percent difference between the ADM and ALM dimensional power fluctuated between 1 and 17%. Contrasting what we observed in Chapter 3, the ALM produces a slightly higher power output than the ADM. The power curve for the model predicts 1.347 megawatts (MW) at 9 m/s. The first turbine in each row is close to this value for both the ADM and ALM, although we observed that the ALM usually over predicts power, whereas the ADM under predicts power.

Figure 28 shows the mean velocity profiles for the ADM and ALM. The wake deficits in the ADM simulation are stronger (shown in dark blue) than the ALM. Figure 29 shows the difference between the ADM and ALM simulations, which was calculated by subtracting the ADM data from the ALM data. The figure reveals that the regions near the center of the wake have the strongest difference (shown in red).

Figure 30 shows wake profiles along rows C and E. The profiles pass through the hub and outboard of the hub in increments of D/8, where D is the rotor diameter. This shows the wake differences between the models at several
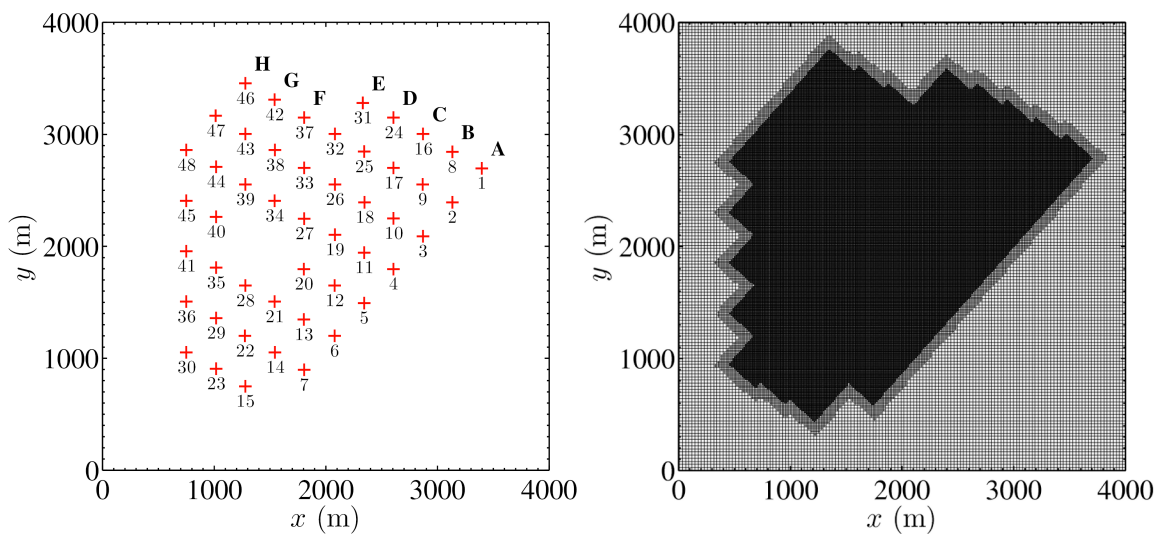
Figure 25. Wind farm layout (left) and computational domain (right). Illustration by Matthew J. Churchfield, NREL.

locations. The biggest difference in wake profiles is on the wake of the first turbine in each row. The ADM creates a larger velocity deficit in the center when passing through the first turbine. The flow begins to recover in the far wake before hitting the next turbines. The ALM and ADM recover to nearly the same value. This pattern repeats until the last turbine in the row. There is a gap in row E, where the flow recovers more than the rest of the turbines. This recovery produces more power on the next turbine in the row, although the flow is not fully recovered. A power production difference of 30% was observed between the turbine right after the gap and the subsequent one. The wake recovery in the gap allows greater power production from the next turbine in the row. Field data always show a slight increase in power of the third turbine over the second turbine in the row. The ALM does not predict this, but the ADM does.

Figures 32, 33, and 34 show wake profiles for turbines 27 through 30, and at 0.5, 0.75, and 1 diameter behind the rotor. The profiles show that the velocity deficit near the center of the wake for the ADM is stronger than that of the ALM. However, moving towards the edge of the wake, the velocity deficit from the ALM is stronger than for the ADM.

The time-step used for the ALM simulation was $\Delta t = 0.015$ s, while the time-step for the ADM simulation was based on a Courant-Friedrichs-Lewy number of 0.75, with typical values close to $\Delta t = 0.06$ s. The difference in time-step may cause the power output differences that were observed. Figure 19 shows that as Δt increases, predicted power decreases, similar to what Figure 27 shows.

The ADM simulation was completed two times faster than the ALM simulation. The ALM simulation required about 1 million CPU-hours, whereas the ADM showed significant savings. This difference is because the ADM has a higher time-step. On a time per time-step basis, the ADM takes longer to calculate all the body forces on the disk (rather than just the body forces on the blades of the ALM).

The ALM and ADM provide similar results in large-scale wind farm simulations. There is a difference in power production, in which the ALM produces more power than the ADM. The difference in the first row of turbines is larger than the turbines that are further downstream. In terms of computational cost, the ADM can be run faster because time-step is not limited to tip speed. The ADM simulation was completed three times faster than the ALM. This time reduction is crucial when performing these type of simulations. The wake in the ADM has a greater deficit

37

in the center than the ALM. However, the velocity deficit near the edges is stronger for the ALM, indicating a larger power extraction is near the outer portion of the blades. The total difference shows that the power extraction for the ALM is greater than that for the ADM.
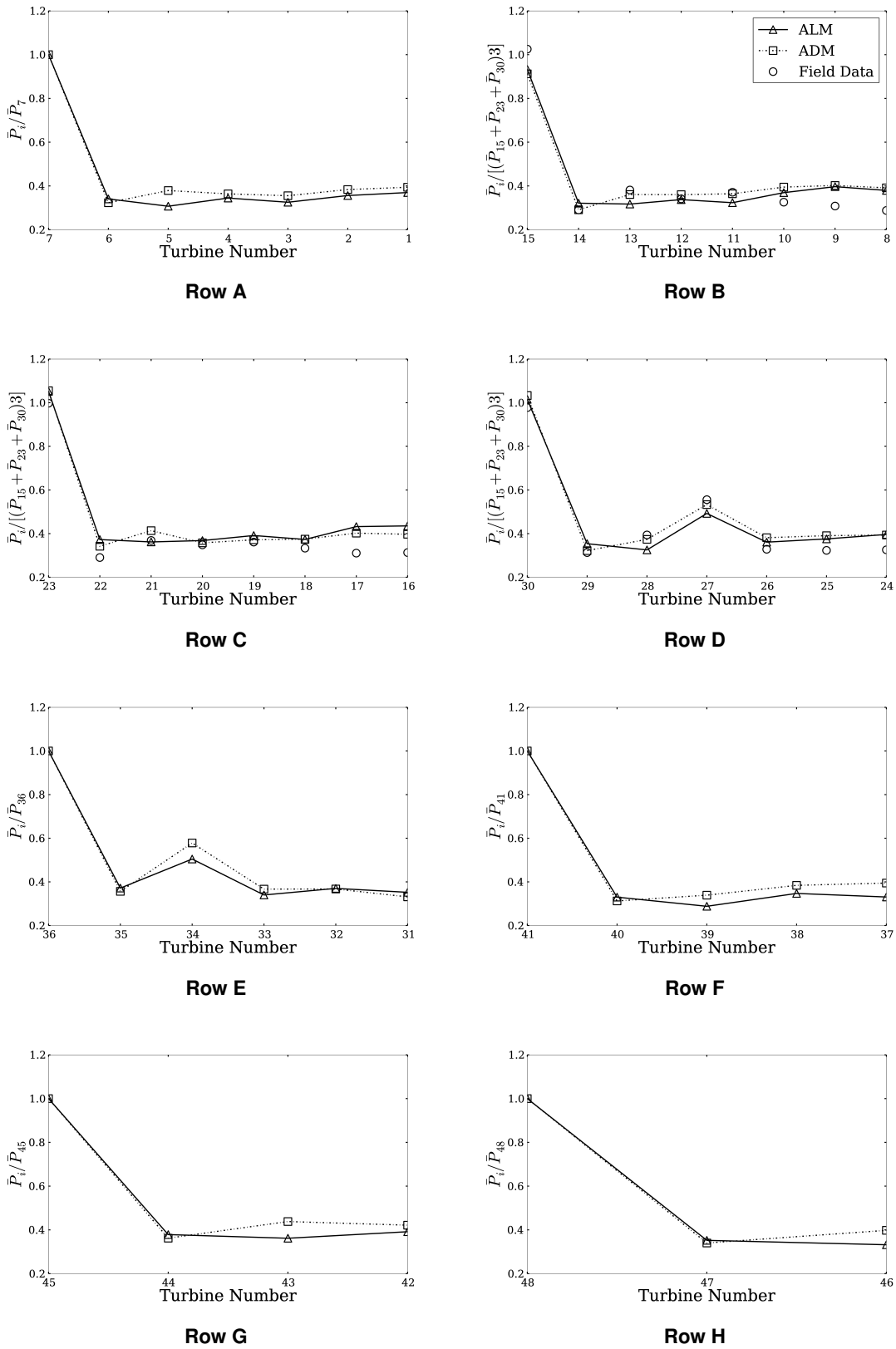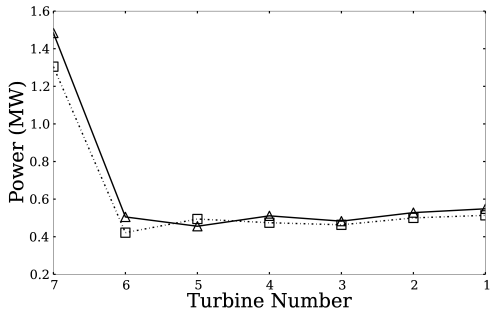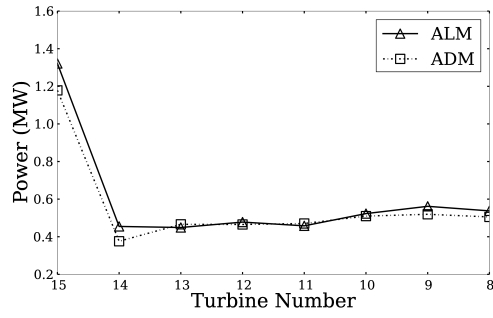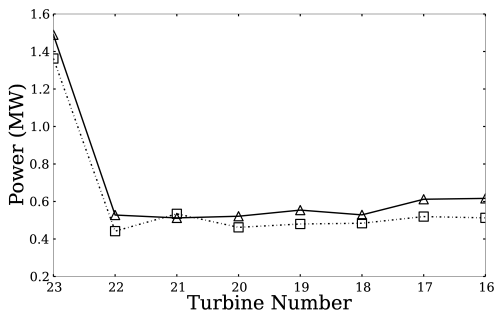
Figure 26. Ten minute average power produced by each turbine, $\bar{P}_i$, normalized by the power of the first turbine in the row. Average over one year of field data is shown for rows B-D.
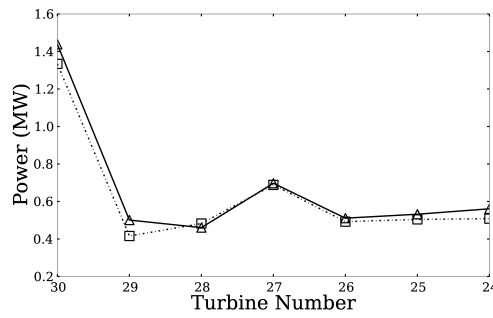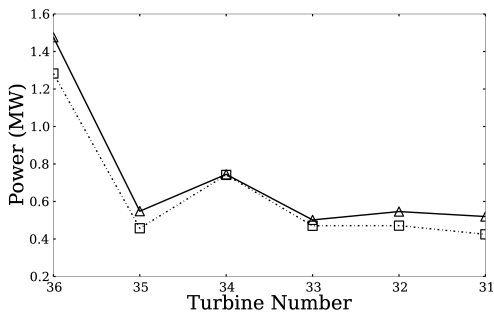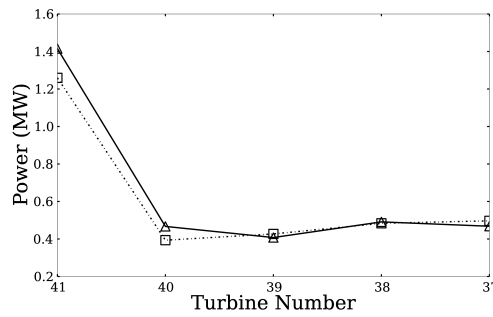
39
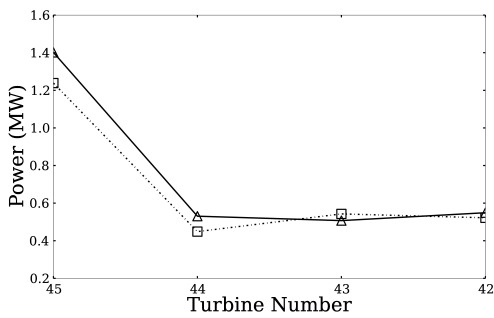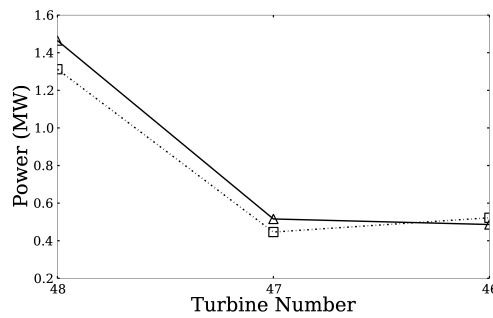
Figure 27. Power produced by each turbine

ADM

ALM
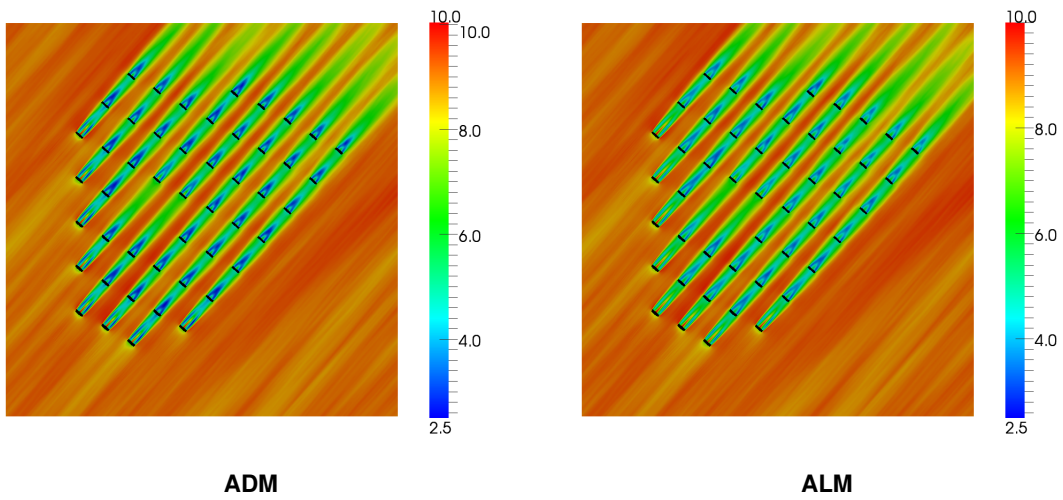
Figure 28. Mean velocity (m/s) contours at hub height for ADM (left) and ALM (right)
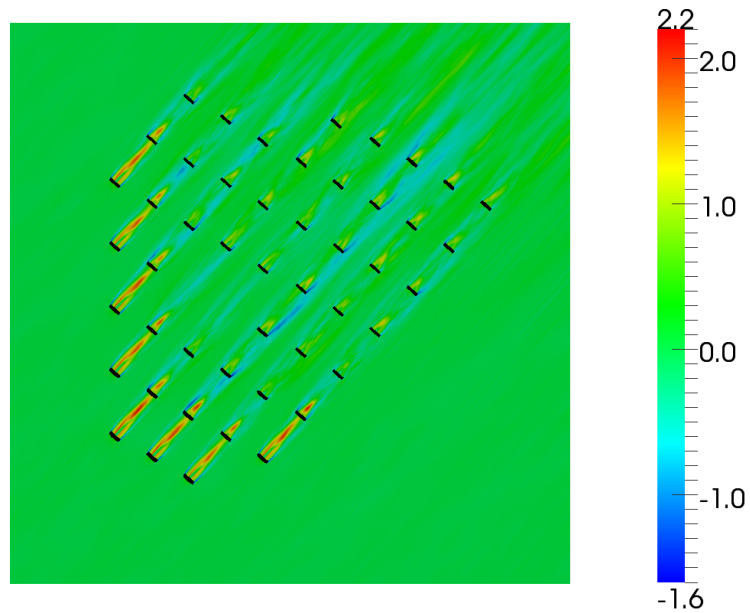
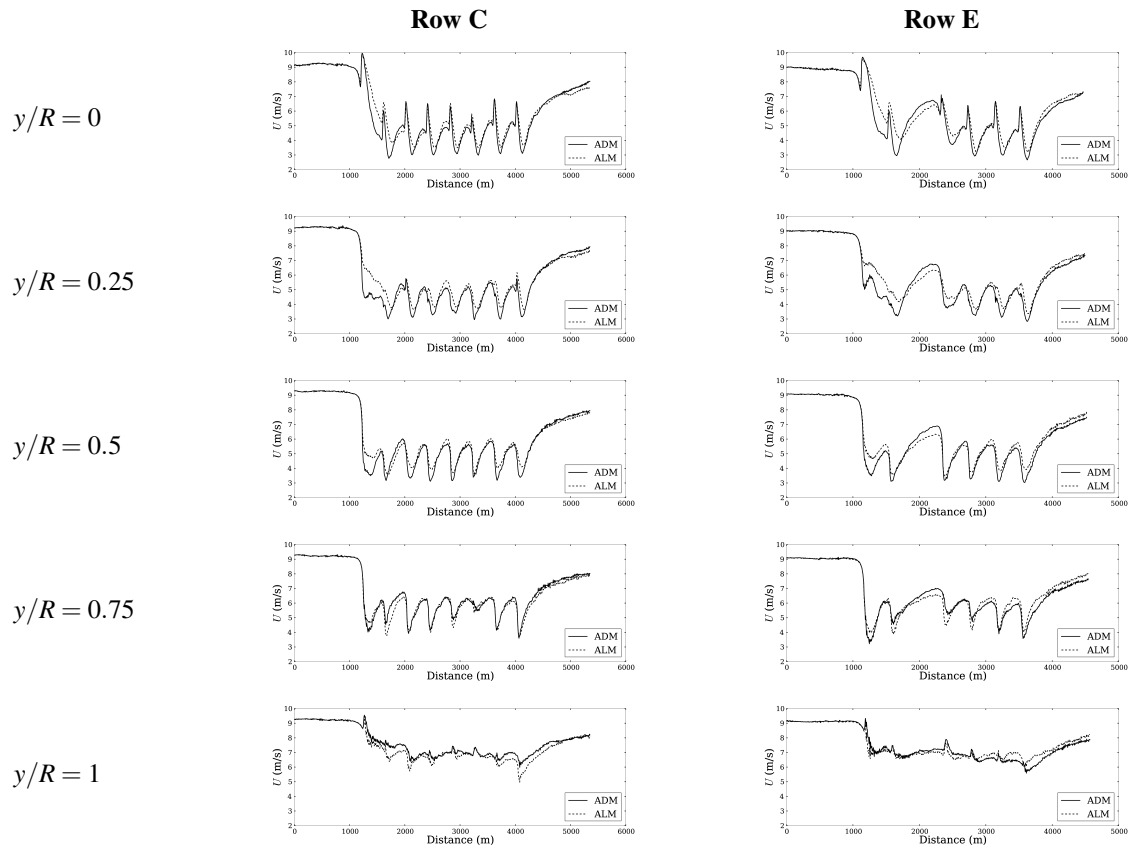**Figure 29. Mean velocity difference (m/s) between ALM and ADM (ALM-ADM)**

41

Row C   Row E

$y/R = 0$

$y/R = 0.25$

$y/R = 0.5$

$y/R = 0.75$

$y/R = 1$

**Figure 30. Mean streamwise velocity profiles at hub height along rows C and E
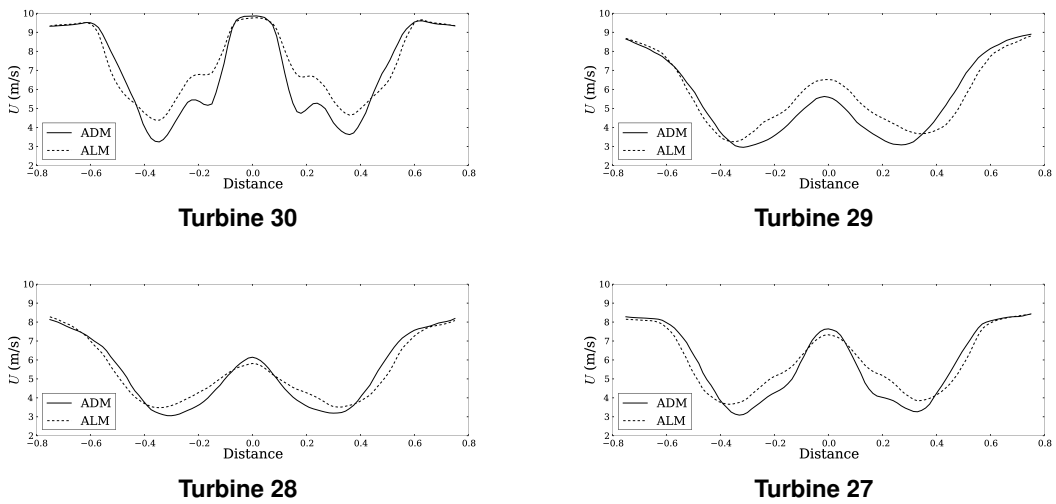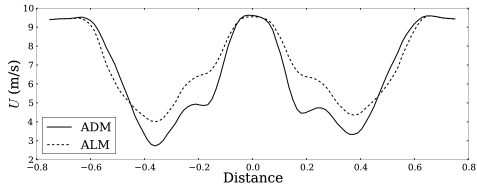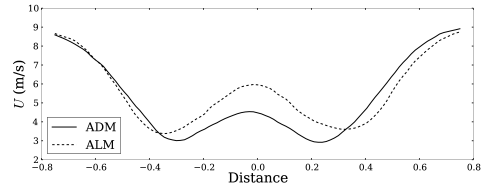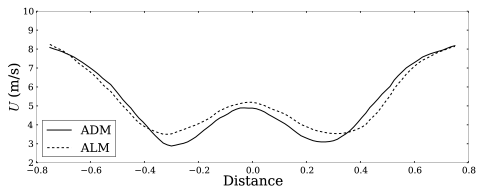at various horizontal locations outboard of hub ranging from hub to blade tip**

Turbine 30   **Turbine 29**

Turbine 28   **Turbine 27**

**Figure 31. Mean velocity in the cross stream direction at
one-fourth diameter behind the rotor for turbines in row D**

42

Turbine 30

Turbine 29
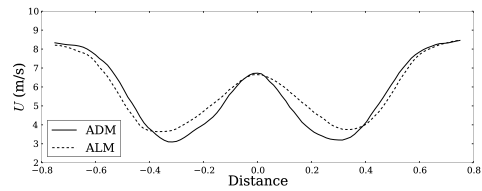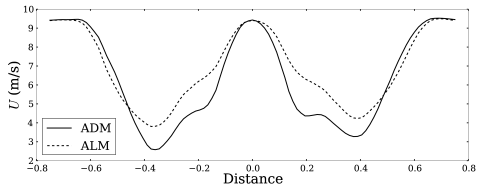

Turbine 28

Turbine 27

**Figure 32. Mean velocity in the cross stream direction at
one-half diameter behind the rotor for turbines in row D**

Turbine 30

Turbine 29

Turbine 28

Turbine 27

**Figure 33. Mean velocity in the cross stream direction at
three-fourths diameter behind the rotor for turbines in row D**

43

Turbine 30

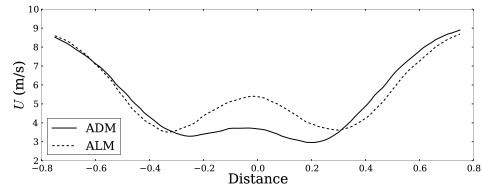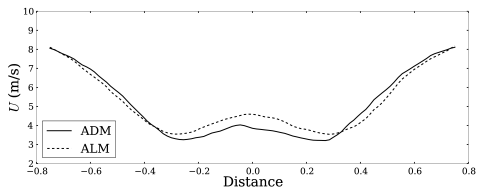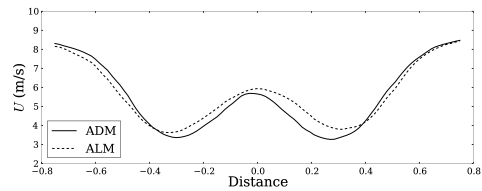**Turbine 29**

Turbine 28

Turbine 27

Figure 34. Mean velocity in the cross stream direction at 1 diameter behind the rotor for turbines in row D

Turbine 30

Turbine 29

Turbine 28

Turbine 27

Figure 35. Mean velocity in the cross stream direction at 3 diameters behind the rotor for turbines in row D

44

Turbine 30

Turbine 29

Turbine 28

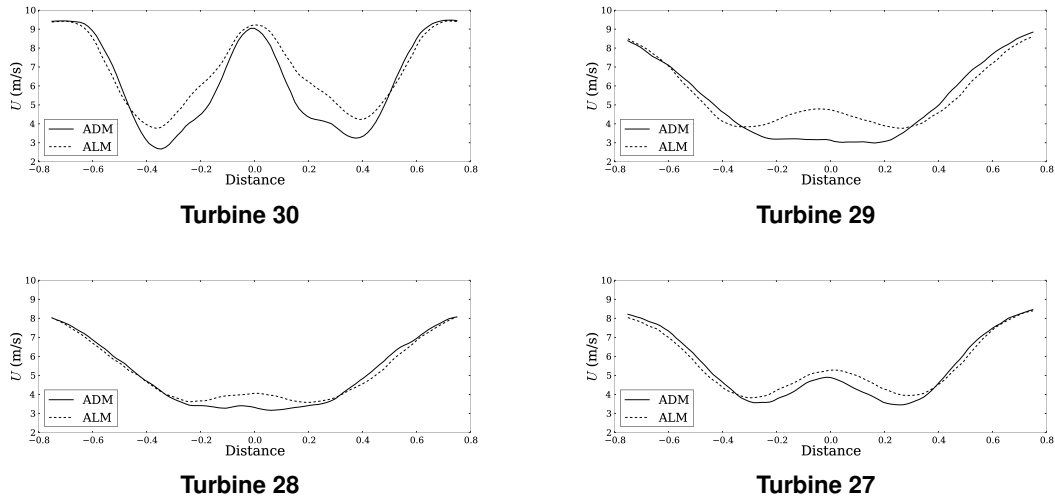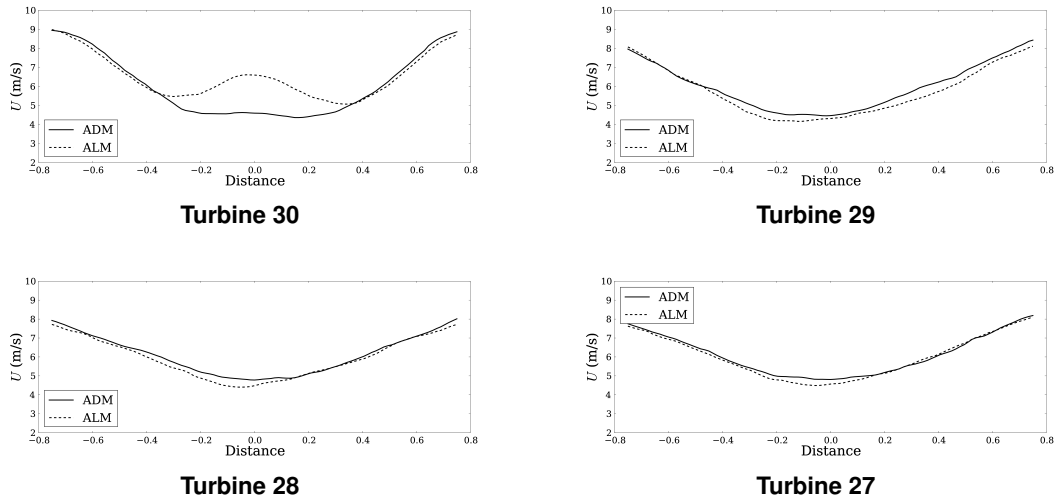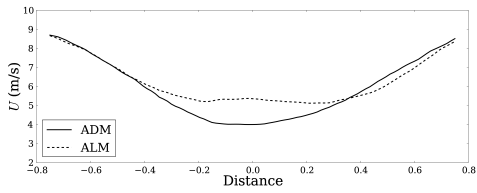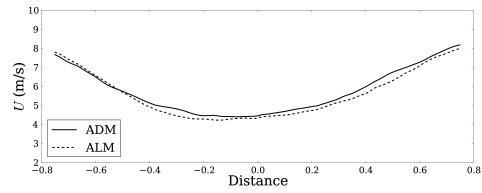**Turbine 27**

Figure 36. Mean velocity in the cross stream direction at 4 diameters behind the rotor for turbines in row D
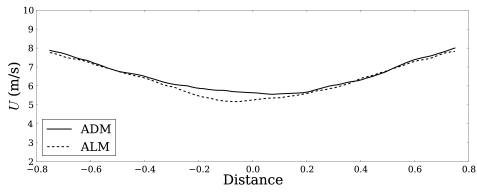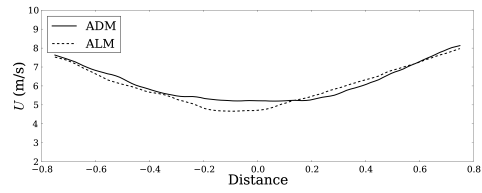
6 Conclusion and Future Work

The actuator line model (ALM) and actuator disk model (ADM) are a suitable representation of a wind turbine when using numerical simulations of fluid flows. The models do not require that the full geometry of the blades be resolved, and, in which case, model them as a set of points in the flow. The ALM models the blades as a set of points along each blade axis, whereas the ADM models the rotor as a disk with points that represent sections of the disk.

The ADM and ALM provide very similar results in simulations with uniform inflow. There is a clear grid dependence on power production and wake profiles of the ADM and ALM. As the grid is refined, the predicted power increases for both models. Using a Glauert tip-loss correction with the ALM decreases the power production. The number of actuator points in the ALM should be adequate to account for all the sections of the blade and provide smooth changes between them. We recommend using a value smaller than $\Delta b/\Delta x = 0.75$. Mean wake profiles are similar for both the ADM and ALM.

A Gaussian function was introduced to avoid numerical instabilities that are caused by the application of forces on discrete sections of the blade. The width of the function was determined by the ε parameter. This parameter played an important role in the models studied. We observed that a parameter closest to the characteristic length of the blade section yielded the best results. As the width of the projection function is decreased, both the ALM and ADM predicted power decreases, but never converges upon a value. A specific value of epsilon allows agreement with blade-element momentum theory predictions. However, the ε parameter must be higher than $2\Delta x$ to avoid numerical instabilities in the solver.

The ALM resolves the flow structures that are caused by the presence of individual blades, which the ADM does not. The ALM matches the physics more closely because it captures the root- and tip-vortices, which the ADM does not. Also, the ALM is able to capture helical and asymmetric structures across the wake, which caused asymmetric roll-up of Kelvin-Helmholtz-like instabilities in the wake's outer shear layer. The ALM captures the vortical structures in the near wake. ADM provides good results in the far wake, but does not produce the vortical structures near the rotor. If simulations are intended to determine the far wake effects, the ADM should provide reasonable results.

We used the ALM to validate a small-scale wind tunnel experiment and compared the structure of the wake for different tip speed ratios. We observed that as the tip speed ratio is higher, the breakdown of the wake occurs faster, leaving a wider wake for larger tip speed ratios. The tunnel walls play an important role in the simulation, as the wake interacts with the walls. The blockage effect of the turbine makes the reference velocity of the tunnel higher near the rotor than on the inlet.

When performing large-scale wind farm simulations, we found that the models perform well. ALM produces slightly more power than ADM under atmospheric boundary layer conditions. It is still unknown why this occurs, but it is possible that the difference is caused by the time-step difference in the simulations. The wake of the ADM is different from that of the ALM. The ADM wake has a stronger wake deficit near the center, whereas the ALM has a stronger wake deficit near the edges. Wake profiles are similar, but we observed that the greatest difference in the near wake, primarily in the first row of turbines.

Bibliography

[1] J.N. Sørensen. Aerodynamics aspects of wind energy conversion. 43:427–448, September 2010.

[2] T. Burton, D. Sharpe, N. Jenkins, and E. Bossanyi. *Aerodynamics of Horizontal-Axis Wind Turbines*, pages 41–172. John Wiley & Sons, Ltd, 2002.

[3] J.F. Manwell, J.G. McGowan, and A.L. Rogers. *Wind Energy Explained: Theory, Design and Application*. Wiley, 2010.

[4] B. Sanderse, S.P. van der Pijl, and B. Koren. Review of computational fluid dynamics for wind turbine wake aerodynamics. *Wind Energy*, 14, 2011.

[5] F. Porté-Agel, H. Lu, and Y.T. Wu. A Large-Eddy simulation framework for wind energy applications. *The Fifth International Symposium on Computational Wind Engineering (CWE2010) Chapel Hill, North Carolina, USA May 23-27*, 2010.

[6] M. Calaf, C. Meneveau, and J. Meyers. Large eddy simulation study of fully developed wind-turbine array boundary layers. *Physics of Fluids*, 22(1):015110, 2010.

[7] N. Troldborg, J.N. Sørensen, and R. Mikkelsen. Numerical simulations of wake charasteristics of a wind turbine in uniform flow. 13:86–99, 2009.

[8] T. Phuoc. Aérodynamique instationnaire turbulente - aspects numériques et expérimentaux. *Journé thématique DRET*, 1994.

[9] N. Troldborg. *Actuator Line Modeling of Wind Turbine Wakes*. PhD thesis, Technical University of Denmark, Lyngby, Denmark, 2008.

[10] I. Ammara, C. Leclerc, and C. Masson. A viscous three-dimensional differential/actuator-disk method for the aerodynamic analysis of wind farms. *Journal of Solar Energy Engineering*, 124(4):345–356, 2002.

[11] A. Jimenez, A. Crespo, E. Migoya, and J. Garcia. Advances in large-eddy simulation of a wind turbine wake. *Journal of Physics: Conference Series*, 75(1):012041, 2007.

[12] C. Masson, A. Smaïli, and C. Leclerc. Aerodynamic analysis of hawts operating in unsteady conditions. *Wind Energy*, 4(1):1–22, 2001.

[13] R. Mikkelsen, J.N. Sørensen, and W.Z. Shen. Modelling and analysis of the flow field around a coned rotor. *Wind Energy*, 4(3):121–135, 2001.

[14] J.N. Sørensen and W.Z. Shen. Numerical modeling of wind turbine wakes. *Journal of Fluids Engineering*, 124(2):393–399, June 2002.

[15] S.S.A. Ivanell, J.N. Sørensen, R. Mikkelsen, and D. Henningson. Analysis of numerically generated wake structures. *Wind Energy*, 12(1):63–80, 2009.

[16] R. Mikkelsen, J.N. Sørensen, S. Øye, and N. Troldborg. Analysis of power enhancement for a row of wind turbines using the actuator line technique. *Journal of Physics: Conference Series – The Science of Making Torque from Wind*, 75(012044), 2007.

[17] R. Mikkelsen. *Actuator Disc Methods Applied to Wind Turbines*. PhD thesis, Technical University of Denmark, Mechanical Engineering Department, 2003.

[18] W.Z. Shen, J.H. Zhang, and J.N. Sørensen. The actuator surface model: A new navier–stokes based model for rotor computations. *Journal of Solar Energy Engineering*, 131(1):011002, 2009.

[19] I. Dobrev, F. Massouh, and M. Rapin. Actuator surface hybrid model. *Journal of Physics: Conference Series*, 75(1):012019, 2007.

[20] C.S. Watters and C. Masson. Modeling of lifting-device aerodynamics using the actuator surface concept. *International Journal for Numerical Methods in Fluids*, 62(11):1264–1298, 2010.

[21] OpenFOAM, Ver. 1.7.1, [available online] Silicon Graphics International Corporation (SGI), URL: http://www.openfoam.org/archive/1.7.1/download/ [accessed 13 December 2011].

[22] J. Smagorinsky. General circulation experiments with the primitive equations. *Monthly Weather Review*, 91:99–164, 1963.

[23] M.J. Buhl. *WT_Perf User's Guide*. National Renewable Energy Laboratory, 2004.

[24] H. Glauert. *Airplane Propellers*, pages 251–268. Dover, New York, 1985.

[25] J. Jonkman, S. Butterfield, W. Musial, and G. Scott. Definition of a 5-MW reference wind turbine for offshore system development. Technical Report NREL/TP-500-38060.

[26] M.S. Adaramola and P.-A. Krogstad. Experimental investigation of wake effects on wind turbine performance. *Renewable Energy*, 36:2078–2086, 2011.

[27] P.-A. Krogstad and J.A. Lund. An experimental and numerical study of the performance of a model turbine. *Wind Energy*, 2011.

[28] D.M. Somers. The S825 and S826 Airfoils Period of Performance : 1994–1995 The S825 and S826 Airfoils. Technical Report January, 2005.

[29] NWTC Design Codes (AirfoilPrep by Dr. Craig Hansen). http://wind.nrel.gov/designcodes/preprocessors/airfoilprep/ [Accessed 21 February 2012].

[30] J.C.R. Hunt, A.A. Wray, and P. Moin. Eddies, streams, and convergence zones in turbulent flows. (1970), 1988.

[31] M.J. Churchfield, S. Lee, P. Moriarty, L.A. Martínez, S. Leonardi, G. Vijayakumar, and J.G. Brasseur. A large-eddy simulation of wind-plant aerodynamics. *50th AIAA Aerospace Sciences Meeting, Nashville, Tennessee, USA*, 2012.

[32] M.J. Churchield. *A Method for Designing Generic Wind Turbine Models Representative of Real Turbines and Generic Siemens SWT-2.3-93 and Vestas V80 Specifications.* National Renewable Energy Laboratory, 2012.